CARDIFF UNIVERSITY
PRIFYSGOL CAERDYDD

ORCA – Online Research @ Cardiff

This is an Open Access document downloaded from ORCA, Cardiff University's institutional repository:https://orca.cardiff.ac.uk/id/eprint/150219/

This is the author's version of a work that was submitted to / accepted for publication.

Citation for final published version:

Ma, Chenglong, Gu, Dongdong, Setchi, Rossitza , Dai, Donghua, Wu, Meiping, Ma, Shuai and Miao, Xiaojin 2022. A large compressive recoverable strain induced by heterogeneous microstructure in a Ni50.6Ti49.4 shape memory alloy via laser powder bed fusion and subsequent aging treatment. Journal of Alloys and Compounds 918 , 165620. 10.1016/j.jallcom.2022.165620

Publishers page: http://dx.doi.org/10.1016/j.jallcom.2022.165620

Please note:
Changes made as a result of publishing processes such as copy-editing, formatting and page numbers may not be reflected in this version. For the definitive version of this publication, please refer to the published source. You are advised to consult the publisher's version if you wish to cite this paper.

This version is being made available in accordance with publisher policies. See http://orca.cf.ac.uk/policies.html for usage policies. Copyright and moral rights for publications made available in ORCA are retained by the copyright holders.

A large compressive recoverable strain induced by heterogeneous microstructure in a $Ni_{50.6}Ti_{49.4}$ shape memory alloy via laser powder bed fusion and subsequent aging treatment

Chenglong Ma[1,2,3,*], Dongdong Gu[4], Rossitza Setchi[5], Donghua Dai[4], Meiping Wu[1,2,3], Shuai Ma[5], Xiaojin Miao[1,2,3]

[1] Jiangsu Key Laboratory of Advanced Food Manufacturing Equipment & Technology, Wuxi, 214122, PR China

[2] Jiangsu Province Engineering Research Center of Micro-Nano Additive and Subtractive Manufacturing, Wuxi, 214122, PR China

[3] School of Mechanical Engineering, Jiangnan University, Wuxi, 214122, PR China

[4] College of Material Science and Technology, Nanjing University of Aeronautics and Astronautics, Nanjing, 210016, PR China

[5] School of Engineering, Cardiff University, CF24 3AA, UK

*Corresponding author. E-mail: Chenglong Ma, chenglongma@jiangnan.edu.cn. Tel.: +86 15298373206

Abstract

Laser induced highly metastable microstructure provides the possibility for the tunable precipitation behavior and mechanical/functional properties via direct aging treatment. In this paper, Ni-rich NiTi-based samples were fabricated by laser powder bed fusion (LPBF) and then were directly aged for different aging times that spanning three time-scales (10 min-100 h). The results showed that through the aging treatment, a heterogeneous microstructure consisting of $Ti_4Ni_2O_x$ nanoparticles, nanoscale Ni-rich precipitates, dislocation structures, and martensitic twin variants formed in the matrix. Due to the change in the elastic strain field, the short time aging treatment tended to induce (001) compound twins, while the long time aging assisted in the formation of <011> type II twins. The temperature-induced and deformation-induced phase transformation behavior were further studied. With the progress of precipitates, it was found that a rapid evolution from a single-stage phase transformation to a multi-stage one occurred. During the cyclic compression, the sample aged for 1 h showed the most excellent superelasticity with initial recoverable strain of 0.089 and steady recoverable strain of 0.087, as well as good cyclic stability.

Keywords: Laser powder bed fusion, NiTi SMAs, aging treatment, microstructure, phase transformation behavior, superelasticity

1. Introduction

NiTi alloys, as the most important practical shape memory alloys (SMAs) with excellent mechanical properties, have a wide range of engineering applications in recent decades, especially in aerospace and medical fields [1-4]. Owing to the temperature or deformation induced reversible martensitic transformation, NiTi SMAs exhibit unique shape memory effect (SME) and superelasticity effect (SE) [1]. It is worth noting that heat treatment has long played an important role in the adjustment of SME and SE for NiTi SMAs, especially for Ni-rich NiTi alloys, since Buehler et al [5] discovered NiTi alloys in1963. The conventional NiTi alloys usually experience a cold working process such as rolling before they are processed into products, which result in the formation of highly anisotropic microstructure with a high density of crystal defects [3, 6]. In this condition, the martensitic transformation is always restricted remarkably. As for Ni-rich NiTi alloys, solution and subsequent aging treatment has been proved to be an effective approach to control the phase transformation behavior and mechanical behavior by the precipitation of Ni-rich intermetallic including Ni_4Ti_3, Ni_3Ti_2 and Ni_3Ti [7-10].

Recently, laser powder bed fusion (LPBF) technology, as the primary metal-based additive manufacturing technology, have got rapidly developed due to the advantages in manufacturing parts with any complex configurations over conventional methods [11]. Hence, increasing interests have been gained in the material-structure-functionality integrated manufacturing of NiTi-based complex parts by using LPBF [12-14]. Different from the conventional processes, the LPBF is a strong nonequilibrium metallurgical process involving ultra-high temperature gradient (10^{5-8} °C/m), huge cooling rate (10^{4-6} °C/s) and complicated stress components within a mesoscale transient molten pool [15]. Meanwhile, cyclic thermal behavior is further created, owing to the

novel materials incremental manufacturing philosophy. Hao et al [16] had found that this unique metallurgical process led to the formation of a highly metastable microstructure containing supersaturated solid solution, a variety of subgrain boundaries, twins and dislocations. Due to the highly metastable microstructure, the LPBF-fabricated Ni-rich NiTi alloys mostly exhibit limited compressive recoverable strain less than 6% after unloading [17]. To enhance the superelastic properties of the LPBF-fabricated Ni-rich NiTi alloys, heat treatment becomes a feasible alternative. But at present, the relative investigations on the heat treatment of LPBF-fabricated NiTi alloys only have limited records. For instance, Hamilton et al [18] studied the effects of aging temperature and time on the transformation temperatures (TTs) of Ni-rich NiTi alloys fabricated by laser direct energy deposition using element powder blends. They substantiated that the TTs of as-deposited Ni-rich NiTi alloys could be systematically controlled by heat treatment. Dadbakhsh et al [19] found that post-annealing might segregate austenite and martensite in the solidified microstructure, although it indeed annihilated the initial large martensite plates. Saedi et al [20, 21] conducted a comprehensive aging study to reveal the effects of aging temperature/time on transformation behavior and deformation behavior. They suggested that the TTs, transformation behavior, strength, and recoverable strain were highly heat treatment dependent. Khoo et al [22] focused on the effect of heat treatment on the transformation strain of LPBF-fabricated NiTi alloys and they found a 400℃-5 min treatment led to an increase of 6.5% in transformation strain. Yang et al [23] obtained a stable tensile recovery strain of 2.25-3.74% by the heattreatment tailoring of the physical properties (e.g. morphology and size) of Ni_4Ti_3 nanoprecipitates. However, the remarkable increase in recoverable strain has not yet been seen. Also, to the best of our knowledge, few investigations have been focused on the direct aging treatment and its influence

mechanism on microstructure, phase transformation behavior and mechanical properties of the LPBF-fabricated Ni-rich NiTi SMAs. During the LPBF, the ultrahigh cooling rate can lead to the formation of the supersaturated solid solution, thereby providing the possibility for the modification via direct aging treatment. The conventional heat treatment for Ni-rich NiTi SMAs normally involves solution and aging. But solution treatment adds an additional step that increases the corresponding time and costs, and also possibly leads to the coarsening of the matrix grains and the loss of strong texture parallel to the building direction (BD) [19].

In this work, Ni-rich NiTi alloy samples were fabricated by LPBF and then were directly aged for different aging times spanning three time scales (10 min-100 h). According to the microhardness evolution feature, three samples aged for 20 min, 1h and 10 h were focused on. Then, the phase transformation behavior, precipitation characteristics, matrix microstructure and superelasticity of these samples were assessed and the relationship among them was elaborated. This work can give more insight into the micro-mechanism for tailoring the superelastic properties of LPBF-fabricated Ni-rich NiTi alloys by the aging treatment, and the effect of longtime heat accumulation on the microstructure during the LPBF of large-scale Ni-rich NiTi alloy components.

2. Experimental procedure

2.1 SLM preparation and aging treatment

The raw material in this study was plasma atomized Ni-rich NiTi pre-alloyed powder with a particle size range from 15-53 μm and a nominal composition of $Ni_{50.6}Ti_{49.4}$ (Fig. 1a). Subsequently, cubic samples with a dimension of 4×4×8 mm^3 and some thin-wall structures were fabricated by using the SLM-150 machine equipped with a 500W IPG ytterbium fiber laser (IPG

Laser GmbH, Germany) (Fig. 1b and 1c). The laser processing parameters in this study were set as follows: laser power of 200 W, scanning speed of 400 mm/s, layer thickness of 30 μm and hatch spacing of 60 μm. A 36° rotation was applied in the scanning directions of adjacent layers during the LPBF process.

After cut from the substrate through the wire-electrode cutting method, some of these cubic samples were put into the furnace for the subsequent aging treatment. The aging treatment was performed using an OTF-1500X tube furnace with single temperature zone (HF-Kejing Co., China) under argon atmosphere. The heating rate of the furnace and the aging temperature were set as 5℃/min and 350 ℃, respectively, according the previous investigations [20, 21]. To study the effects of aging time on the microstructures and properties of LPBF-fabricated NiTi SMA samples, a wide aging time range was involved, including 10 min, 20 min, 40 min, 1 h, 1.5 h, 3 h, 5 h, 10 h, and 100 h (Fig. 1d). As-aged samples were shown in Fig. 1e.

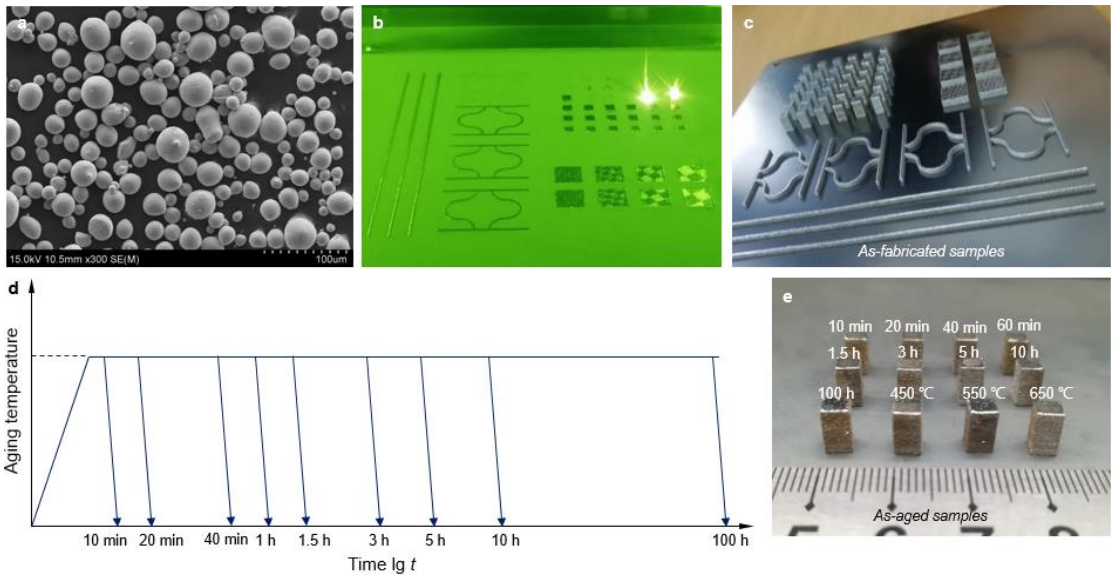

Fig.1 a The raw powder material showing a high degree of sphericity; **b** The LPBF process showing the interaction between laser beam and powder bed; **c** The as-fabricated samples; **d** The aging treatment regime; **e** The as-aged samples.

2.2 Material characterization

The DSC 3 (METTLER TOLEDO, Switzerland) differential scanning calorimetry (DSC) was used with a heating and cooling rate of 10 ºC/min from -50 ºC to 150 ºC, to obtain the phase transformation temperatures (M_s, M_f, A_s and A_f) of as-aged NiTi samples. Here M_s, M_f, A_s and A_f denote the austenite-to-martensite transformation start temperature, austenite-to-martensite transformation finish temperature, martensite-to-austenite transformation start temperature and martensite-to-austenite transformation finish temperature, respectively. As for the detailed microstructures of as-aged samples, the transmission electron microscope (TEM) and high-resolution TEM (HRTEM) were carried out by using a Tecnai G2 F20 S-TWIN (operated at 200 kV) (FEI. co., the USA) to analyze the nanoscale precipitates, dislocations and twins. What's more, the superelasticity was assessed based on cyclic compressive tests that were conducted on a CMT5205 testing machine (MTS Industrial Systems, China) at a cross head velocity of 1 mm/min. The testing temperature was at room temperature. The Vickers microhardness was measured using an HXS-1000AY microhardness indenter (AMETEK, China) with a load of 100 g and a dwell time of 15 s. Five parallel microhardness values for any one in two typical regions (namely the interior region and boundary region of the molten pool) of each sample were given, in order to guarantee the reliability of testing data.

3. Results

3.1 Microhardness evolution

Fig. 2 gives the microhardness evolution of as-aged Ni-rich NiTi SMAs with the aging time. It was found that the change trends of microhardness values in the interior zone and the boundary zone were similar (Fig. 2a). Besides, the average microhardness value in the interior zone was

apparently lower than that in the boundary zone. Three apparent hardening peaks corresponding to the aging time of 20 min, 3 h and 10 h were observed. The maximum average microhardness values emerged when 20 min of aging was applied, reaching 338.8 $HV_{0.1}$ in the interior zone and 401.4 $HV_{0.1}$ in the boundary, respectively. When the aging time increased from 20 min to 1 h, the average microhardness values in the interior zone and the boundary zone dramatically decreased to 234.9 $HV_{0.1}$ and 253.1 $HV_{0.1}$. As the aging time was more than 10 h, the average microhardness in the above two different zones achieved a steady state, which showed 325.2 $HV_{0.1}$ and 356.8 $HV_{0.1}$ at 100 h, respectively. Fig. 2b compares the hardening behavior of NiTi alloys processed by different manufacturing methods as a function of aging time [20, 21, 24-27]. For the NiTi alloys processed by the conventional methods such as cold-drawing or arc melting, the microhardness evolution curve is relatively simple, usually showing a single hardening peak. However, for the additive manufactured NiTi alloys, the microhardness evolution curve is complex where more hardening peaks might exist. Accordingly, it can be concluded that the microhardness evolution with the aging time strongly depends on material composition (mainly Ni concentration) and material processing history.

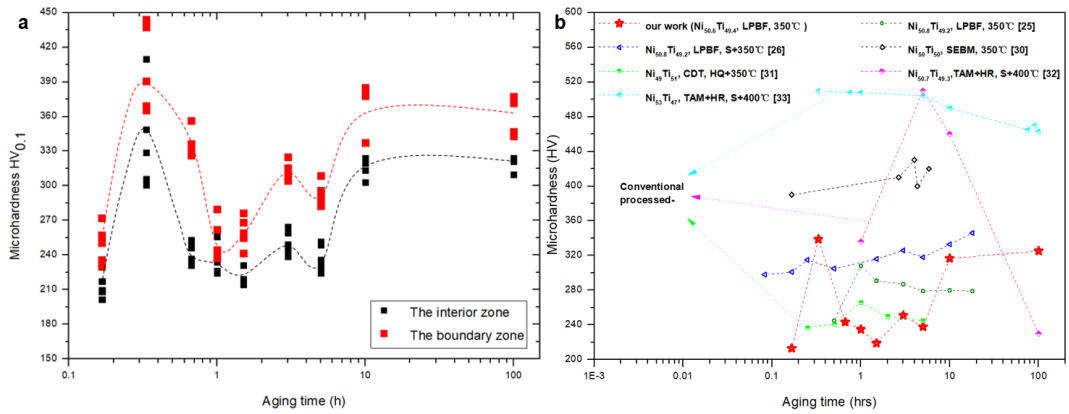

Fig. 2 Microhardness evolution with the aging time. **a** The measured microhardness values in the interior zone and boundary zone of the molten pool at different aging time; **b** Comparisons with

other investigations [20, 21, 24-27]. Here, SEBM is selective electron-beam melting, CDT means cold-drawn and tempered, TAM denotes tungsten arc melting; HQ is the homogenized and quenched state, S means solution.

3.2 Phase transformation behavior

Fig. 3 depicts the DSC curves of the Ni-rich NiTi samples obtained at different aging times, aimed to reveal the effect of aging time on the phase transformation path and temperature. The detailed characteristic temperature data (M_s, M_f, A_s *and* A_f) and heat of transformation (Q) from all peaks (peak 1-6) in the DSC curves were summarized in **Table 1**. For comparison, the DSC curve of as-fabricated NiTi sample was also given. It clearly showed two independent peaks corresponding to the heating process (B19'→B2) and the cooling process (B2→B19'), respectively. The M_s of the forward transformation (A→M) was as low as 21.41 ℃, which indicated that the B2 phase dominated in the solidified microstructure. The temperature intervals (ΔT) for the forward and reverse transformations reached 62.98 ℃ and 65.15 ℃, respectively. As the aging time came to 20 min, the sample kept a single transformation path but the peak temperatures of the forward and reverse transformations were remarkably elevated to 44.75 ℃ and 90.89 ℃, respectively. Meanwhile, the temperature interval for the phase transformation became much broader. When the aging time was increased to 1 h, multi-stage martensitic transformation started to occur, with appreciably decreased transformation characteristic temperatures and temperature interval. For this emerged multi-stage transformation, the forward transformation path could be described as B2 →B19' and B2 →R, as well as the reverse one contained B19'→R→$B2_1$ and B19' →$B2_2$. The R↔B2 reversible transformation could be identified by the very small temperature hysteresis in the DSC curve. Allafi et al [8] pointed out

that the emergence of the multi-stage transformation meant the existence of inhomogeneous composition distribution within the aged sample. As the aging time further got extended from 1 h to 10 h, the transformation peaks kept a continuous shift to higher temperature, synchronously with the gradually sharpened peak configuration. Additionally, it was found that the precursory B19'→R in the reverse transformation process was almost completely suppressed in the 10 h aged sample. This meant considerable R phase formed in this case.

Table 1 A summary about characteristic temperature data (M_s, M_f, A_s *and* A_f) and heat of transformation (Q) from all peaks (peak 1-6 marked in Fig. 3) in the DSC curves of as-fabricated sample and as-aged samples.

Aging time t (h)	Forward martensitic transformation							Reverse martensitic transformation						
	Temperature (°C)				Heat (J/g)			Temperature (°C)				Heat (J/g)		
	M_s^1	M_f^2	M_s^3	M_f^3	Q^1	Q^2	Q^3	A_s^4	A_f^5	A_s^6	A_f^6	Q^4	Q^5	Q^6
0	21.41	-41.6	-	-	18.68	-	-	-	-	-13.2	51.94	-	-	17.30
0.333	67.85	11.70	-	-	20.17	-	-	-	-	64.79	112.22	-	-	16.38
1	47.62	31.89	-	-	8.28		0	36.51	47.91	73.03	95.24	9.49		1.85
3	51.23	36.47	-	-	11.02		0	39.96	51.07	73.91	99.17	9.35		3.66
5	52.78	38.58	-	-	9.12		0	42.26	52.18	82.95	95.52	9.12		0.87
10	54.99	41.13	8.50	-7.2	9.35		0.31	45.38	53.92	85.83	96.79	5.30		0.65

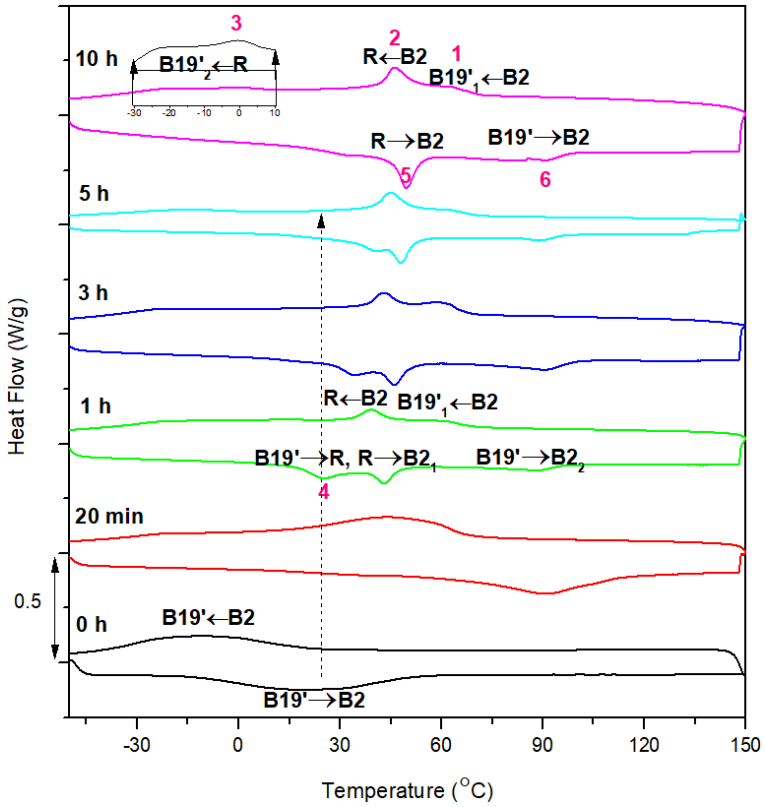

Fig. 3 DSC curves of the Ni-rich NiTi samples obtained at different aging times. 1, 2 and 3 denote the transformation peaks emerging in the forward transformation process; 4, 5 and 6 denote the transformation peaks emerging in the reverse transformation process.

Fig. 4a further demonstrates the variations in the characteristic temperatures (M_s^1, M_f^2, A_s^4, A_f^5, A_s^6 and A_f^6) with the aging time. It was showed that M_s^1, A_s^4 and A_f^6 demonstrated a similar variation trend with the aging time, including a decrease stage and a slight increase stage, while M_f^2 and A_s^6 kept a continuous increase with the aging time. Note that, it was clear that the inflection points of almost all characteristic temperature evolution curves occurred at 1 h of aging. Besides, the overall transformation hysteresis $\Delta T_H = A_f^6 - M_s^1$ and the heat of the forward and reverse transformation, Q_{for} and Q_{rev}, are plotted as a function of aging time, as shown in Fig. 4b. As for the ΔT_H, a remarkable increase could be observed as the aging time changed from 0 to 3 h, which was followed by a steep reduction since longer aging time than 3 h was applied. The heat

of the forward and reverse transformation basically kept a declining trend with the aging time, except for the case at 3 h of aging when a slight rebound occurred.

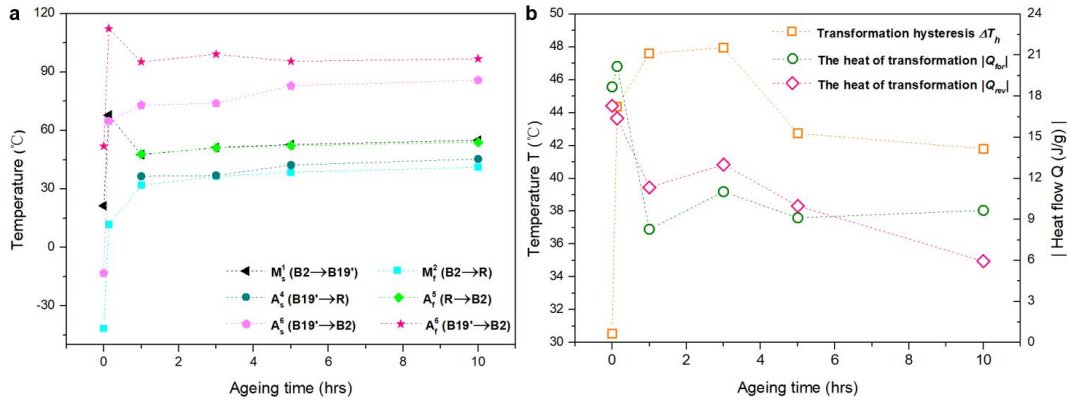

Fig. 4 Effect of aging time on (**a**) the characteristic temperatures, (**b**) transformation hysteresis and the heat of the forward and reverse transformation.

3.3 Superelastic behavior

Fig. 5 depicts the cyclic compressive deformation behavior of as-fabricated and as-aged samples at ambient temperature. All samples were loaded up to the fixed 1000 MPa and then were unloaded until the stress was decreased to zero. Fig. 5a displays the cyclic compressive stress-strain curves. The result showed that with the aging time increasing, the recoverable behavior present a complicated evolution. But after 10 cycles, all samples became completely recoverable at ambient temperature, free of any residual strain. Figs. 5b and 5c further give the evolutions of the maximum strain ε_{max}, the initial recoverable strain $\varepsilon_{initial\text{-}rec}$, the steady recoverable strain $\varepsilon_{steady\text{-}rec}$, the quasi-plateau stress σ_c and quasi-plateau strain ε_c at different aging time. As for the as-fabricated sample, an excellent superelasticity was obtained with almost negligible residual strain. The $\varepsilon_{initial\text{-}rec}$ was 0.068 and even the $\varepsilon_{steady\text{-}rec}$ reached 0.065, both of which were higher than 0.06. Besides, no apparent plateau stage appeared in the curve and consequently the enveloped area was very small. When 20 min of aging was applied, the residual strain still kept a relatively limited

value but the $\varepsilon_{initial\text{-}rec}$ got remarkably increased to 0.085. Also, the forward stress quasi-plateau appeared and the σ_c showed a relatively high value of 485 MPa. As the aging time further increased to 3 h, the cyclic curve formed with a drastically decreased σ_c (~180 MPa) and apparent residual strain after unloading. In this case, the $\varepsilon_{initial\text{-}rec}$ was only 0.048. However, when the applied aging time came to 10 h, a noteworthy improvement of the superelastic property at ambient temperature was observed, with an appreciably increased $\varepsilon_{initial\text{-}rec}$ reaching 0.087. But in this condition, the σ_c was elevated to 297 MPa again.

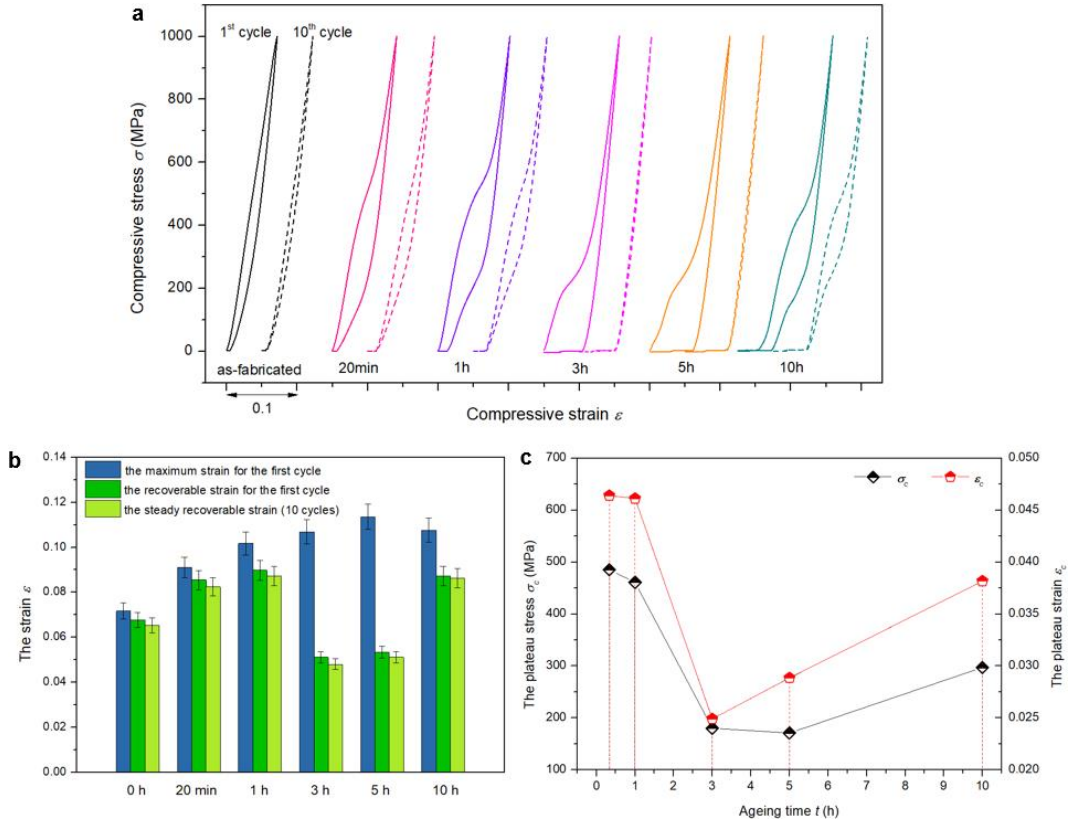

Fig. 5 The superelastic behavior of as-fabricated sample and as-aged samples. **a** The cyclic compressive loading-unloading curves; **b** The variations in the maximum strain and the recoverable strain at different aging time; **c** The evolutions of the plateau stress σ_c and the plateau strain ε_c.

3.4 Microstructure features

Based on the effects of aging time on microhardness, phase transformation temperature and superelastic behavior of the LPBF-fabricated NiTi alloy, we further chose the samples aged for 0 h, 20 min, 1 h and 10 h to carry out the microstructure characterizations. Fig. 6 displays the TEM images and their corresponding selected area diffraction patterns (SADPs) of the matrix microstructures of the chosen samples. As for the as-fabricated sample, the microstructure was mainly characterized with columnar B2 grains and the corresponding SADP showed that the incidence direction was parallel to $\{001\}_{B2}$ (Figs. 6 a1 and a2). Besides, a certain density of dislocations were observed in the matrix and most of these dislocations existed with a shape of "*V*" due to the pinning effect from the second phase particles. After 20 min of aging, lath-like martensite B19' formed within the matrix (Figs. 6 b1 and b2). The B19' showed a crystal orientation relationship of $[001]_{B2}$ // $[-321]_{B19'}$ with the B2 phases. Additionally, strip-like dislocation wall structures instead of dispersed dislocations in the as-fabricated sample formed and their length could reach several hundred nanometers. Due to the existence of martensite, apparent kinking phenomena for the dislocation walls occurred in the interface of B2/B19' (Fig. 6 b1). As the aging time increased to 1 h, many fine acicular martensitic twin lamellas formed within the lath-like martensite (Fig. 6 c1), simultaneously exhibiting a crystal orientation relationship of $[100]_M$ // $[10\text{-}1]_T$ (Fig. 6 c2). These martensitic twins belonged to (001) compound twins where the twin plane was (001) and the twin direction was [100], which could be confirmed by the information from the relative investigations such as Ezaz et al' s work [28]. Meanwhile, the density of dislocations in this condition seemed to get decreased apparently and these dislocations tended to form at the interfaces between twins. Furthermore, in some local areas, the segregated R-phase microstructure was observed (Figs. 6 c3 and c4) with two typical different variants. The

crystal orientation relationship between the matrix and R phase met $[001]_{B2}$ // $[011]_{R}$. At 10 h of aging, the <011> type II twins instead of (001) compound twins formed. Two sets of type II twins consisting of an acicular variant and another coarsened variant distributed in a decussate pattern (Figs. 6 d1-d3). Moreover, the R-phase microstructure was also detected (region D) and the corresponding SADP is shown in Fig. 6 d4. Meanwhile, high density of dislocations formed in this condition (Fig. 6 d1), mainly distributing nearby the martensitic twin boundaries.

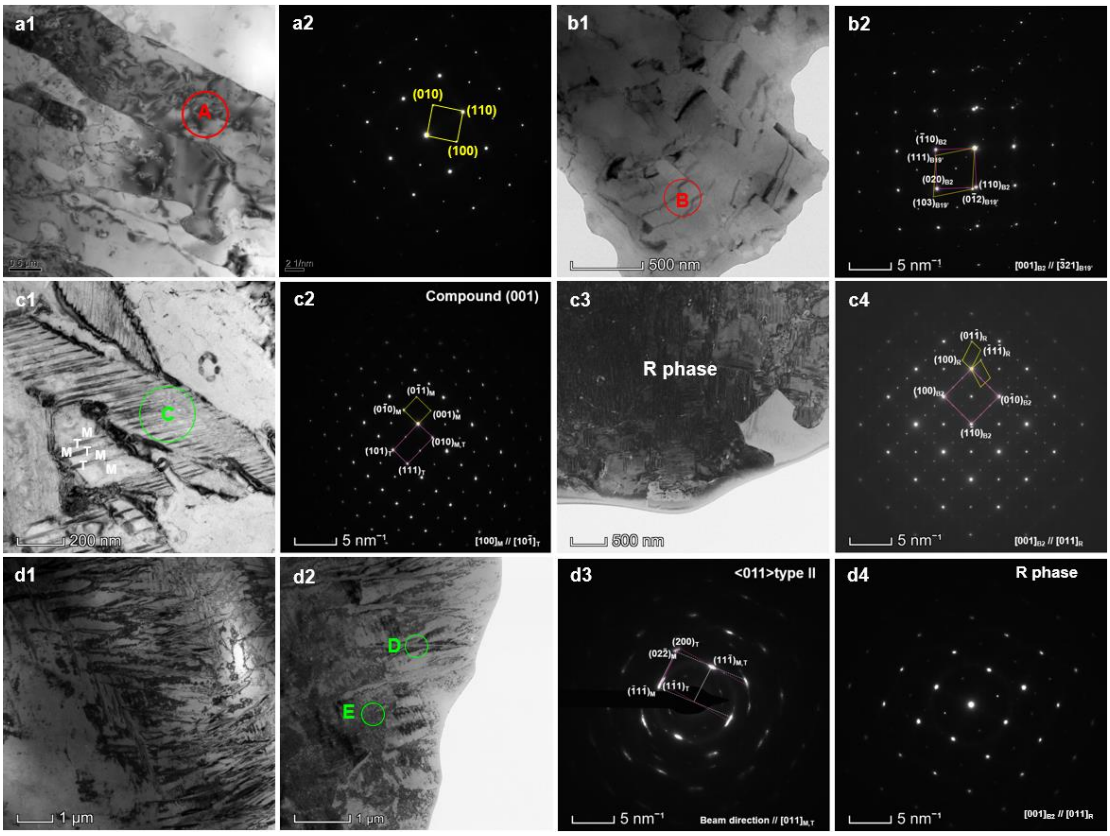

Fig. 6 TEM images and the corresponding SADPs of the microstructure in the as-fabricated and as-aged samples. **a1-a2** as-fabricated sample, **a1** the TEM image and **a2** the SADP of region A; **b1-b2** 20 min aged sample, **b1** the TEM image and **b2** the SADP of region B; **c1-c4** 1 h aged sample, **c1** the TEM image showing the fine acicular martensitic twin lamellas, **c2** the SADP of region C, **c3** the TEM image showing the R phase and **c4** the corresponding SADP; **d1-d4** 10 h aged sample, **d1** and **d2** the TEM images captured in two different zones, **d3** and **d4** the SADPs of

region D and region E, respectively.

Apart from the aged martensite, we also studied the changes in the type, morphology, size and composition of the second phase particles or precipitates during the aging process. $Ti_4Ni_2O_x$ particle as the typical second phase particle is always observed in the solidified microstructure of the LPBF-fabricated NiTi alloy, due to the inevitable Ni evaporation effect and the element segregation within the molten pool [16, 29, 30]. Fig. 7 shows the changes of the morphology and composition of $Ti_4Ni_2O_x$ particle, as well as the interfacial structure between the matrix and $Ti_4Ni_2O_x$ particle. In the as-fabricated sample, the average size of $Ti_4Ni_2O_x$ particle was only ~15 nm (Fig. 7a and b) and the interfacial structure was semi-coherent with a ~8.4% misfit degree (Fig. 7c). However, for the aged samples, the observed $Ti_4Ni_2O_x$ particle existed with a strip-like shape and the maximum size reached ~80 nm (Fig. 7d and e). This might be associated with the continuous growth of adjacent particles. Besides, with the aging time increasing, the *x* in the $Ti_4Ni_2O_x$ nanoparticle kept rising due to the diffusion of oxygen element (Fig. 7d-f). Consequently, an amorphous interface structure was formed (Fig. 7e). When the aging time comes to 10 h, part of $Ti_4Ni_2O_x$ particles were transformed into TiO_x particles (Fig. 7f) under the severe oxygen invasion and the aging environment (350℃).

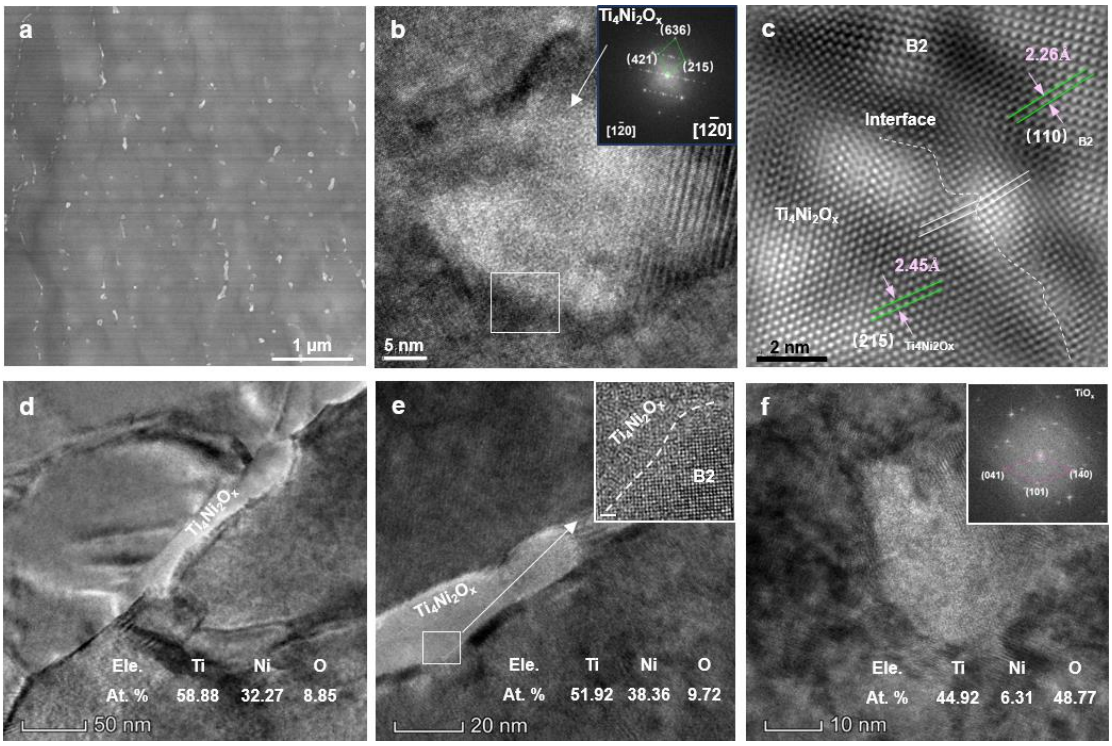

Fig. 7 Morphology and chemical content of the $Ti_4Ni_2O_x$ nanoparticle in different conditions. **a-c** the $Ti_4Ni_2O_x$ nanoparticle existing in the as-fabricated sample and **a** the SEM image showing the distribution feature of $Ti_4Ni_2O_x$ nanoparticles along the grain boundaries, **b** the HR-TEM image showing a single $Ti_4Ni_2O_x$ nanoparticle, **c** the inverse FFT images showing the interface structure. **d-f** corresponding to the $Ti_4Ni_2O_x$ nanoparticle observed in the 20-min, 1-h and 10-h aged samples, respectively.

As the main product during the aging treatment, the precipitation and evolution of the Ni_4Ti_3 intermetallic phase were naturally focused on. Fig. 8 depicts the evolution of the Ni_4Ti_3 phase in the precipitate size and the interfacial structure at different aging time. In the 20 min aged sample, many fine lenticular Ni_4Ti_3 particles with a length of ~10 nm and a thickness of ~3 nm were found to distribute along the B2 grain boundary (Figs. 8a and 8b). Meanwhile, these fine Ni_4Ti_3 shared a coherent interface with the B2 matrix (Fig. 8c). As the aging time increased to 1 h, many Ni_4Ti_3 variants emerging in the interior of the grains were also observed and showed a remarkably

increased precipitate diameter more than 500 nm (Fig. 8d). However, when the aging time came to 10 h, the precipitate density of Ni_4Ti_3 apparently became lower and meanwhile the previous coherent interface between Ni_4Ti_3 and B2 was transformed to semi- or non-coherent one (Figs. 8e and 8f).

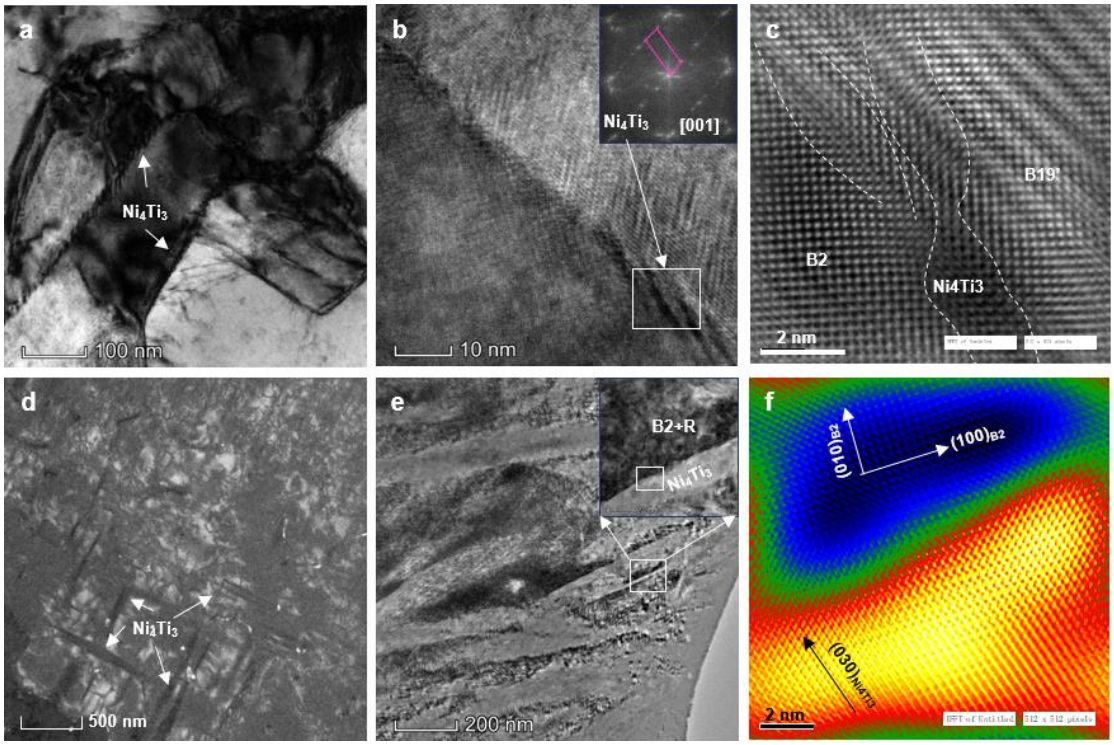

Fig. 8 TEM characterization of the Ni_4Ti_3 precipitate at different aging time. **a-c** the HR-TEM, FFT and inverse FFT images of Ni_4Ti_3 precipitates at the B2 grain boundaries in the 20 min aged sample; **d** the dark-field TEM image of Ni_4Ti_3 precipitates in the 1 h aged sample; **e** and **f** the HR-TEM and inverse FFT images of Ni_4Ti_3 precipitates in the 10 h aged sample.

4. Discussion

It is found that different treatment conditions give rise to the formation and growth of different Ni-rich or Ti-rich precipitates. The referred treatment conditions include the LPBF and the aging treatments for different aging time. The LPBF and subsequent aging treatment mainly involve the rapid solidification process and complex solid state phase transformation process. Fig.

9 is presented to illustrate these two processes well. During the rapid solidification stage, due to the strong thermal undercooling and constitutional undercooling, Ti_2Ni preferentially precipitates from the undercooling melt. Then, the supersaturated NiTi B2 phase dominates in the solidified microstructure. During the subsequent aging stage, considerable martensitic phases including B19' and R-phase instead of the B2 phase emerge in the as-aged samples. Additionally, different types and sizes of Ni-rich intermetallic compounds also precipitated from the matrix. From the DSC results, it is also shown that the evolution of a single B19'↔B2 transformation to the B19'↔R↔B2 multiple transformation stream occurs with aging time increasing. These are just indicative of the switching over from the relatively homogeneous microstructure to the multi-phase heterogeneous microstructure. At the optimized aging condition, this heterogeneous microstructure further result in the specific phase transformation behavior and a large compressive recoverable strain. In the following sections, we will discuss the microstructural evolution mechanism, formation mechanism of multi-stage phase transformation and physical mechanisms of excellent superelasticity.

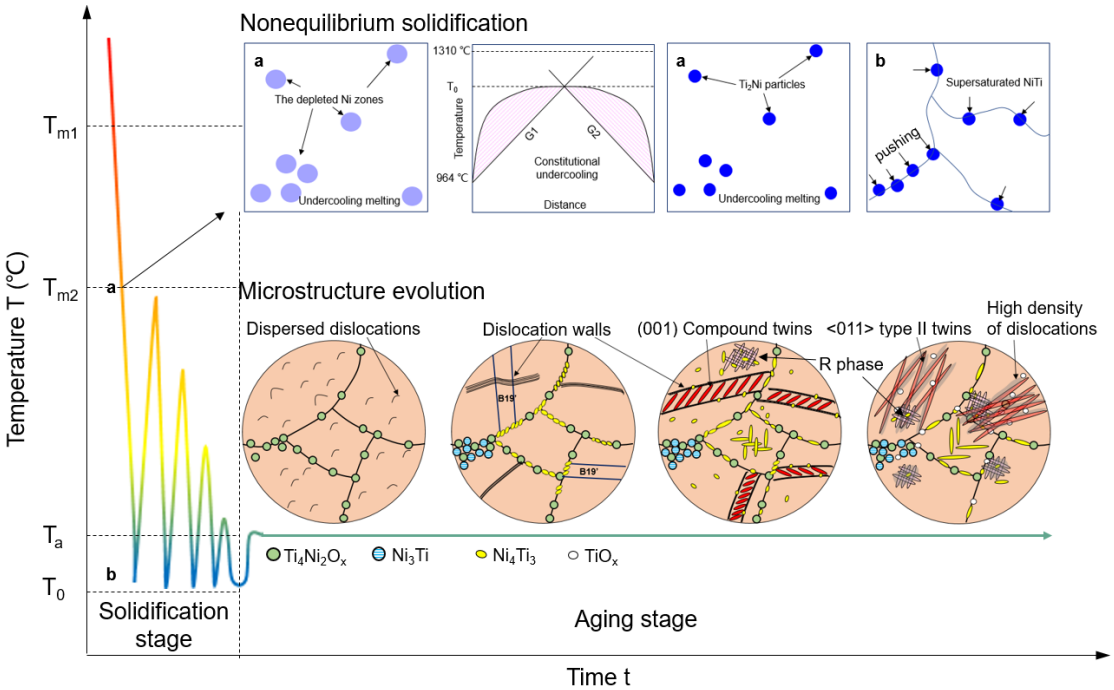

Fig. 9 The thermal history and evolution process of microstructures during the LPBF and subsequent aging treatment. Tm_1, melting temperature of NiTi phase, Tm_2, melting temperature of Ti_2Ni phase, T_a, aging temperature and T_0, ambient temperature.

4.1 Microstructural evolution mechanism in aging treatment stage

4.1.1 The development of precipitates and dislocations

As for the LPBF process, homogeneously distributed $Ti_4Ni_2O_x$ nanoparticles is the main precipitate phase. Because the raw powder is slightly Ni-rich ($Ni_{50.6}Ti_{49.4}$), it can be deduced that the formation of $Ti_4Ni_2O_x$ derives from the significant Ni evaporation. Due to the Gaussian distributed energy density of laser beam and the scattering effect in the powder bed, the Ni evaporation randomly occurs in some local zones, consequently leading to heterogeneous distribution of the depleted Ni zones within the molten pool. This inhomogeneous distribution feature of Ni element can be described based on Klassen's multi-component evaporation model [31]. In views of the very limited solubility of Ti in NiTi and the strong undercooling induced by the LPBF, Ti_2Ni phase can precipitate prior to NiTi phase nucleation (as shown in Fig. 9) [32]. On the other hand, owing to the high reaction activity of Ti component with oxygen as well as the high solubility of O in Ti_2Ni phase [33], Ti_2Ni is partly transformed into $Ti_4Ni_2O_x$ phase which unevenly distributes in the undercooled melt. During the subsequent solidification, $Ti_4Ni_2O_x$ particles are trapped by the moving NiTi boundaries. Hence, $Ti_4Ni_2O_x$ particles are inclined to distribute along the matrix grain boundaries. The existence of $Ti_4Ni_2O_x$ nanoparticles in turn further causes the enrichment of Ni concentration within the surrounding matrix.

Strong inhomogeneity of Ni element distribution in the as-fabricated sample further brings about the heterogeneous precipitation in the subsequent aging treatment process. For instance, in

20 min aged sample, direct precipitation of Ni_3Ti phase with typical stacking faults was found in some local zones (Fig. 10a), rather than a gradual equilibrium transition of $Ni_4Ti_3 \rightarrow Ni_3Ti_2 \rightarrow Ni_3Ti$ with increasing aging time in normal conditions [7]. Even the precipitation of Ni_3Ti phase had happened, the surrounding matrix still exhibited high Ni content of 52.09 at. %. It was also observed that these segregated Ni_3Ti particles precipitated and grew attaching to the Ti_2Ni particles (Fig. 10b), which was consistent with Hou et al's work [34]. For other zones with relatively low Ni concentration, the Ni atoms tend to migrate toward the grain boundary where Ni_4Ti_3 possesses a higher nucleation rate (Figs. 8a) [35].

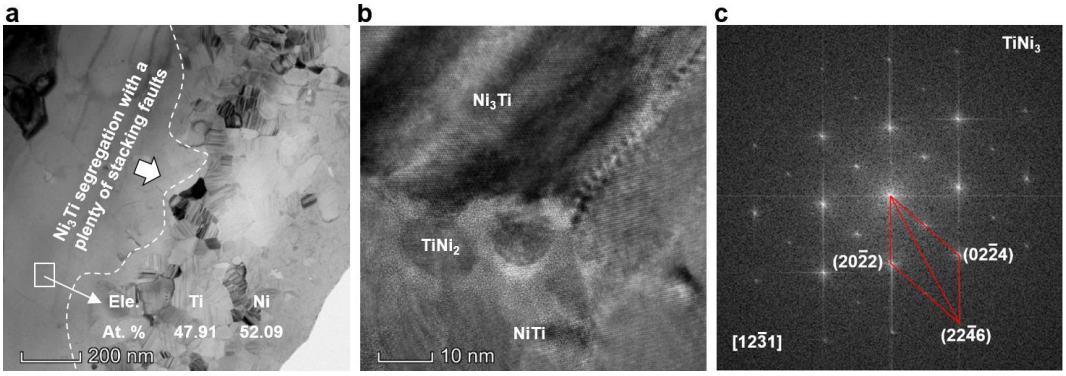

Fig. 10 TEM characterization of Ni_3Ti particles. **a** TEM images, **b** the local high-resolution TEM image and **c** the corresponding FFT image of the Ni_3Ti precipitate in the 20 min aged sample.

Fig. 11 depicts the dislocation structure features at different treatment conditions. In the LPBF-fabricated NiTi, a great many dispersed dislocations could be observed (Fig. 11a). These dislocations mostly showed the wave morphologies consisting of many connected segments, due to the complicated dislocation reactions during the solidification process [16]. The formation of these dislocations can be attributed to the internal stress and high concentration of vacancies [36]. Due to a sufficient supersaturation of vacancies in the matrix induced by the strong undercooling during the laser processing, dislocations can be produced by the generation, aggregation and collapse of vacancies [37]. Based on the calculation, the dislocation density at room temperature

can be roughly estimated as ~10^{10}/cm^2. However, in the aging stage, the dislocation structure and density changed significantly. Fig. 11b shows the dislocation morphology in 20 min aged sample. Different from the dispersed dislocations inside grains for the as-fabricated sample, the dislocations in the 20 min aged sample were bunched together and emerged in a form of dislocation wall or tangle. It can be deduced that the dislocation motion plays an important role in this process. The driving force of the dislocation motion mainly originates from two aspects, including the thermal activation provided by the aging temperature to decrease the energy barrier, and the osmotic force generated by the local vacancy subsaturation which forms during the precipitation of Ni_4Ti_3 nanoparticles [38]. As the aging time extends, the dislocation density gradually rise and its distribution becomes heterogeneous, as shown in Fig. 11c and d. In these two cases, the multiplication of dislocations is the key factor. Simon et al [39] found the stress field induced by an approaching acicular martensite could activate an in-grown dislocation segment and generate characteristic narrow and elongated dislocation loops, during the martensitic transformation that creates the $\{001\}_{B19'}$ compound twins. These dislocations forming at the B2/B19' interfaces can help to facilitate strain compatibility [40]. Besides, by increasing aging time, a loss of the coherent interface with the growth of the precipitates can be also a source of dislocation multiplication. These dislocations originated from diverse sources can interact with each other by the dislocation motion, thus facilitating the formation of a high density of dislocation structures.

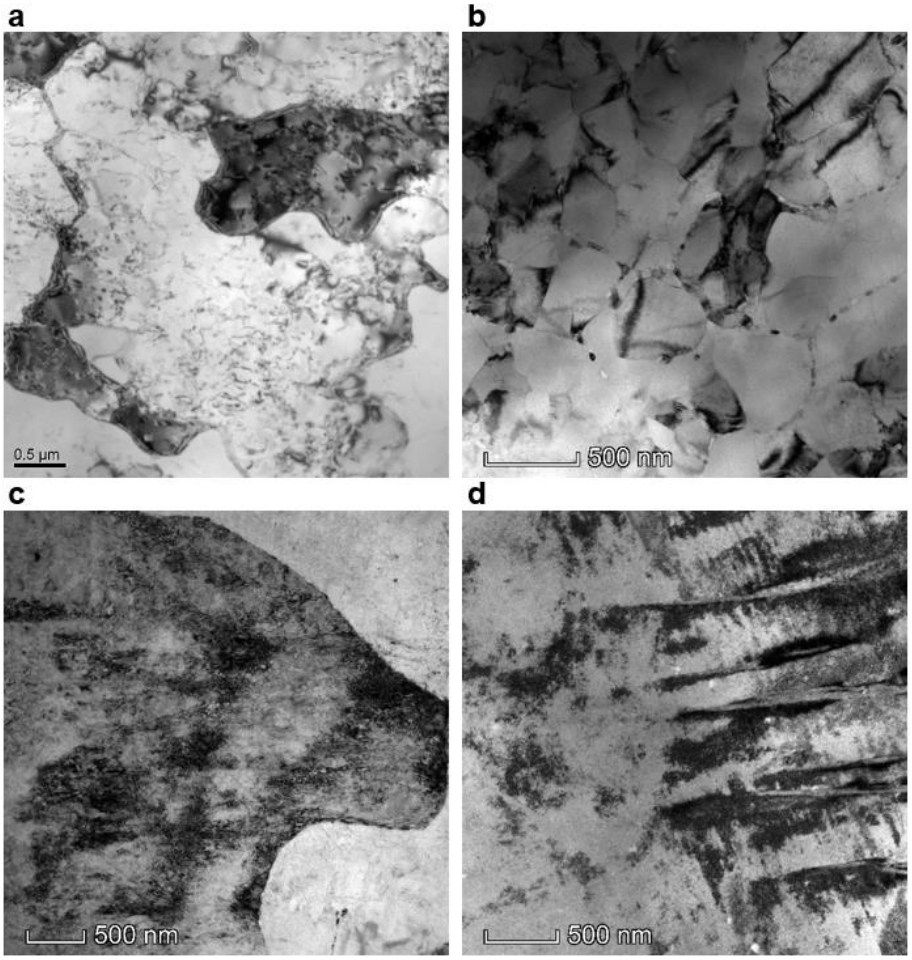

Fig. 11 TEM images of dislocations observed in the LPBF-fabricated and aged NiTi samples. **a** as-fabricated sample, **b** 20 min aged sample, **c** 1 h aged sample, and **d** 10 h aged sample.

4.1.2 Formation mechanism of the aged martensitic twins

Different from the near full B2 phase microstructure in the as-fabricated sample, the aged samples show the characteristic martensitic twin microstructure. Based on the martensitic phenomenological thermodynamics, the thermodynamical equilibrium equation of martensitic transformation can be described as:

$$\Delta G^{A-M} = \Delta H^{A-M} - T\Delta S^{A-M} + \Delta E_{el}^{A-M} + \Delta E_{ir}^{A-M} = 0 \quad (4\text{-}1)$$

where ΔE_{el}^{A-M} is the elastic strain energy, ΔE_{ir}^{A-M} is the inelastic strain energy or the friction energy. $(\Delta H\text{-}T\Delta S)^{(A\text{-}M)}$ is the chemical Gibbs free energy change of martensitic transformation, regarding as the driving force, while $(\Delta E_{el}+\Delta E_{ir})^{(A\text{-}M)}$ is connected with the transformation barrier.

To guarantee the occurrence of martensitic transformation, the $(\Delta E_{el}+\Delta E_{ir})^{(A\text{-}M)}$ is required to be as low as possible. Here ΔE_{ir}^{A-M} mainly derives from A/M interface friction and plastic work within A/M interfaces due to their coherency loss. A decrease of ΔE_{ir}^{A-M} could be realized through increasing the nucleation sites of martensite that reducing the interfacial motions, i.e. Ni-rich precipitates [34]. As for ΔE_{el}^{A-M}, Stroz et al [41] further expressed it as follows, when no external stress is applied.

$$\Delta E_{el}^{A-M} = \sum_{i\,j}\left(-\frac{1}{2}\sigma_{ij}^{t}\,\varepsilon_{ij}^{t} - \sigma_{ij}^{d}\,\varepsilon_{ij}^{t}\right) \tag{4-2}$$

where σ_{ij}^{t} and σ_{ij}^{d} are the internal stress caused by the transformation and the defects or precipitates, respectively, ε_{ij}^{t} is the transformation strain. Zhou et al [42] pointed out the ε_{ij}^{t} ($\boldsymbol{r}$) could be described by the combined effect of the concentration field $c(\boldsymbol{r})$ and structural order parameter field $\eta(\boldsymbol{r})$ in the matrix:

$$\varepsilon_{ij}^{t}(\vec{r}) = \chi^{B2}\delta[c(\vec{r}) - c^{eq}][1-\eta(\vec{r})] + \varepsilon_{ij}^{p}[\eta(\vec{r})] \tag{4-3}$$

where $\chi^{B2}=\Delta a/(a\cdot\Delta c)$ is the lattice expansion coefficient of the B2 matrix, δ is the Kronecker delta function, and c^{eq} is the equilibrium Ni concentration of the B2 matrix. For the order parameter η, there exist two limits, namely (i) if η=0, the ε_{ij}^{t} ($\boldsymbol{r}$)=$\chi^{B2}\delta[c(\boldsymbol{r})\text{-}c^{eq}]$, which indicates the transformation strain relies on the Ni concentration of the matrix; (ii) if η=1, the ε_{ij}^{t} ($\boldsymbol{r}$)= ε_{ij}^{p} ($\boldsymbol{r}$) means the intrinsic strain induced by the precipitated particle.

For the LPBF-ed sample, due to the steep temperature gradient within the molten pool, the significant internal stress can be generated to trigger the martensite transformation, according to our previous study [43]. However, in this work, excessive Ni atoms is solubilized into B2 matrix so that the nucleation barrier is enough large to suppress the transformation. During the aging process, with the development of precipitates and dislocations, the Ni concentration and the elastic

strain fields within the matrix vary, therefore influencing the subsequent martensitic transformation and attendant aged microstructure. Waitz et al [44] have indicated that specific dislocation configurations (such as dislocation walls or pile-ups) or the coherent particles might act as possible nucleation sites. For the 20 min aged sample, a significant change in Ni content within the matrix occurs, with the precipitation of Ni_3Ti and Ni_4Ti_3. According to Eqs. (4-2) and (4-3), a considerable decrease of Ni content leads to a low transformation strain and attendant small transformation barrier. Especially for the matrix at the molten pool boundaries, in virtue of the larger residual internal stress and possible nucleation sites, the martensite plates form and subsequently grow until being terminated at the grain boundaries. When the aging time extends to 1 h, an apparent growth of the Ni_4Ti_3 precipitates can be found. Simultaneously with the dislocation multiplication and motion, the elastic strain field in the matrix gets enhanced significantly, further resulting in the formation of the (001) compound twins during the furnace cooling. Normally, the compound twinning occurs in the case associated with large stress and strain to accommodate additional straining, since it is not a lattice invariant shear. However, M. Nishida et al [45] also found the existence of the (001) compound twins in an aged Ti-51 at.% Ni SMA. Compared with some other twins (i.e. type II twins or {20-1} type twins) that requires combined shear and shuffle, (001) twins that can be created by shear alone is preferred due to its lower fault energy and the smaller twinning shear magnitude (0.2385) calculated by Ezaz et al [28]. On the other hand, due to the precipitation of more coherent Ni_4Ti_3 variants in this condition, R phase transformation with the smaller transformation strain occurs accordingly. When the aging time comes to 10 h, the Ni_4Ti_3 precipitates get coarsened apparently, thus leading to a loss of Ni_4Ti_3/B2 coherent interface and a decrease of precipitate density. As a result, the formation

conditions for the compound twins are not available. During the subsequent furnace cooling, martensitic transformation occurs naturally, owing to the low Ni concentration and a decrease of η. But due to the accumulated high density of dislocations, the migration of the B2/B19' interface encounters considerable barrier and consequently the <011> Type II twins instead of compound twins form to minimize the total interfacial energy, which is consistent with Nishida et al's work [45]. Besides, the accumulated high density of dislocations in this condition can also further facilitate the nucleation of R phase, according to Fukuda et al's work [46].

4.2 Formation mechanism of multistage phase transformation

To give more insight into the change in TTs and transformation paths, the Landau free energy is involved, which can be written as an appropriate 2-4-6 potential [47]:

$$F = a(T - T^*)\eta^2 - b\eta^4 + c\eta^6 \quad (4\text{-}4)$$

where a(>0), b(>0), c(>0) are coefficients dependent on composition, T^* is the harmonic instability temperature. In consideration of the linear relation between F and T, the Eq. (4-4) can be further simplified as F=U-TS, entropy S is the slope of the F-T line. During the martensitic transformation, the corresponding entropy change could be described simply as ΔS=-$a(\eta_M)^2$ according to the Eq. (4), where η_M is the lattice distortion at TT. Hence, $\Delta S(T=T_M)$ is relation to the change in the slope of the F-T line, indicating the deviation between the F_{B2} and $F_{B19'}$. As shown in Fig. 12, the schematic of the reasonable transformation paths and temperatures at different aged conditions is illustrated. For the LPBF-fabricated sample, due to the formation of supersaturated solid solution B2 phase, the matrix only shows a single transformation path B2↔B19' with a relatively low TT (Fig. 12a). Note that, owing to inhomogeneous Ni content distribution, the DSC curve emerged with a wide TT region (Fig. 3). After 20 min aging treatment,

accompanied with the precipitation of Ni-rich phases, Ni content in the matrix and resultant transformation strain (Eq. (4-3)) get decreased apparently. The previous investigations have pointed out that the intrinsic transformation strain for B19' and R is ~10% and ~1%, respectively. Thus, a decrease of Ni content strongly influences the free energy of B19' but less influences the free energy of R, as shown in Fig. 12b. In this condition, the transformation still occurs in the form of single path B2↔B19', but the TT is pushed to a high position. As the aging time gets increased to 1 h, the elastic strain energy in the matrix tends to be apparently enhanced, according to the earlier discussion. In this stage, the effect of the variation in elastic strain energy on transformation strain is more remarkable, comparing with the decrease of Ni content due to the growth of Ni_4Ti_3. Then, the free energies of three phases are pulled back to some degree, in relation to the positions in Fig. 12b. Due to the higher sensitivity to an increase of elastic energy [41], the amplitude of the increase in the value of $F_{B19'}$ is larger than that of F_R (Fig. 12c), thus triggering the multistage transformations (B2↔R↔B19'). As the aging time is further prolonged, the Ni content in the matrix continuously decreases with the growth of Ni-rich precipitates, therefore to some extent reducing the free energies of three phases (Fig. 12d). As a result, the TTs get intensified, by comparison with those in Fig. 12c. When more aging time is applied, the oxygen invasion into the matrix becomes remarkable, consequently consuming Ti element in the matrix. A balance between the decrease in Ni content induced by the growth of Ni-rich intermetallic phases and the increase in Ni content induced by the oxidation is reached. But it is observed that the B19'↔R transformation is apparently suppressed after long time aging (Fig. 3), which can be attributed to an increase of dislocation defects acting as the nucleation sites of R phase. In this condition, the free energies of three phases can be described by Fig. 12e, thus accounting for the occurrence of

the dominated R transformation (10 h) in DSC curves.

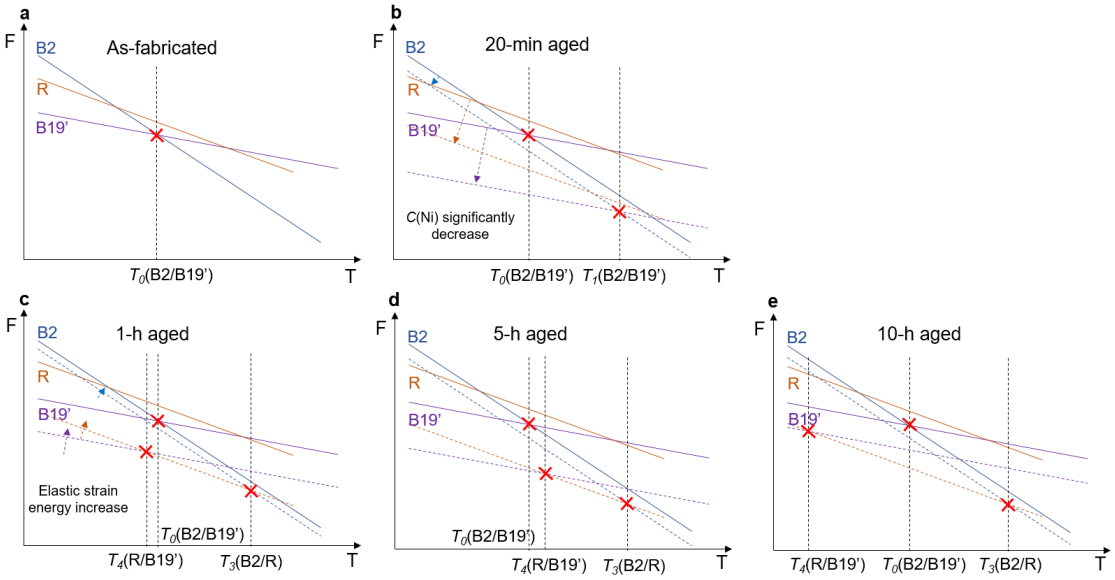

Fig. 12 The Landau free energy of B2, B19' and R phases at different aging conditions, disclosing the change in the reasonable transformation path and temperature.

4.3 Physical mechanisms of a large compressive recoverable strain

For the superelastic behavior of NiTi samples, the most crucial index is the recoverable strain. We compare the results with the reported data from the as-fabricated or heat-treated NiTi alloys in different loading conditions (e.g. 600, 800, 1000, and 1200 MPa) [17, 21, 48-51], as shown in Fig. 13. Our LPBF-fabricated $Ni_{50.6}Ti_{49.4}$ alloy simultaneously exhibits the highest initial recoverable strain and steady recoverable strain, reaching 0.0677 and 0.0653, respectively. It is indicated that limited irrecoverable stain accumulation during the cyclic loading-unloading process occurs. Of particular significance is that the optimized aging treatment can further remarkably improve the recoverable strain. The measured largest steady recoverable strain in the aged state reaches 0.0872, 58.5% higher than the reported largest value. The increase in recoverable strain arises from the multiple physical mechanisms, including orientation texture, $Ti_4Ni_2O_x$ nanoparticle and nanoscale coherent Ni_4Ti_3 precipitate.

For the LPBF-fabricated sample, the large recoverable strain is achieved mainly via the special orientation texture and the $Ti_4Ni_2O_x$ nanoparticle. The intrinsic mechanism lies in the increases of the critical resolved shear stress (CRSS) and the Schimid factor for slip. In the bcc-B2 dominated matrix, the slip systems include (011)[0-11], (001)[010], (-211)[-101], (011)[1-11] and (011)[001]. The (011)[001] slip system is the predominance due to the lowest energy barrier [52]. Although the EBSD characterization is not performed in this work, our previous work has found that the strong orientation texture {001}//BD //loading direction (LD) existed in the as-fabricated sample [43]. Hence, the Schmid factor for the (011)[001] slip system is calculated to be zero under compressive loading, which means that it is difficult for the activation of the (011)[001] slip system, thereby minimizing the plastic deformation and improving the superelasticity. Besides, the preferentially precipitated $Ti_4Ni_2O_x$ nanoparticle can significantly enhance the CRSS or the yield strength of the LPBF-fabricated NiTi alloy, by the modulus hardening effect. The relative detailed descriptions can be available in our previous work [43] and the strengthening contribution can reach ~265 MPa.

For the aged samples, the enhanced recoverable strain can be mainly attributed to the heterogeneous microstructure. In essence, it results from a decrease in the critical stress for stress induced martensitic transformation (SIMT) (Fig. 5a) and a further increase of the CRSS (Fig. 2a). Our recent work [52] pointed out that the SIMT was not homogeneous during the whole loading process, thus resulting in a low recoverable strain. In this work, the aging treatment induced heterogeneous microstructure mainly consisting of $Ti_4Ni_2O_x$ nanoparticles, nanoscale Ni-rich precipitates, martensite twins and supersaturated B2 phase, can contribute to a more homogeneous SIMT. On one hand, considerable Ni-rich particles such as Ni_4Ti_3 and Ni_3Ti precipitated from the

matrix result in an apparent decrease in Ni concentration in the matrix, which efficiently lower the nucleation barrier of SIMT during the compressive loading. On the other hand, the plenty of fine coherent Ni_4Ti_3 nanoparticles as well as the small amounts of aged martensite can act as the martensitic nucleation sites to facilitate the reversible martensitic transformation during the loading-unloading cycle. Besides, these precipitated fine Ni-rich particles also enhance the slip resistance via the dispersion strengthening, thus giving rise to enhanced cyclic stability and resultant large steady recoverable strain.

However, at an improper aging time such as 3 h or 5 h, the recoverable strain shows a sharp decrease. The martensite with various compound twin variants can be responsible for this significant decrease. During the compressive loading, a much lower stress is only required for the reorientation and growth process of the (001) twins, because the corresponding migration energy cost is only ~7.6 mJ/m^2 [28]. With the growth of the (001) twins, high internal stresses stemming from a network of interface might trigger the occurrence of slip to facilitate the strain compatibility, considering that only 20 mJ/m^2 of barrier magnitude is required for the initiation of (001) slip [53]. As the external stress increases, the {201} twins and {113} twins can appear successively by consuming the compound twins. Upon unloading, these deformed twins are retained, thereby resulting in an apparent increase of residual strain. But when the aging time comes to 10 h, the aged martensitic microstructure is mainly featured as the <011> type II twins and R phase. Due to the existence of high density of dislocations, these dislocations can serve as nucleation sites to reduce the energy barrier for the A→M, R→M forward transformations during the loading and the reverse transformations during the unloading. Consequently, the recoverable strain gets improved apparently.

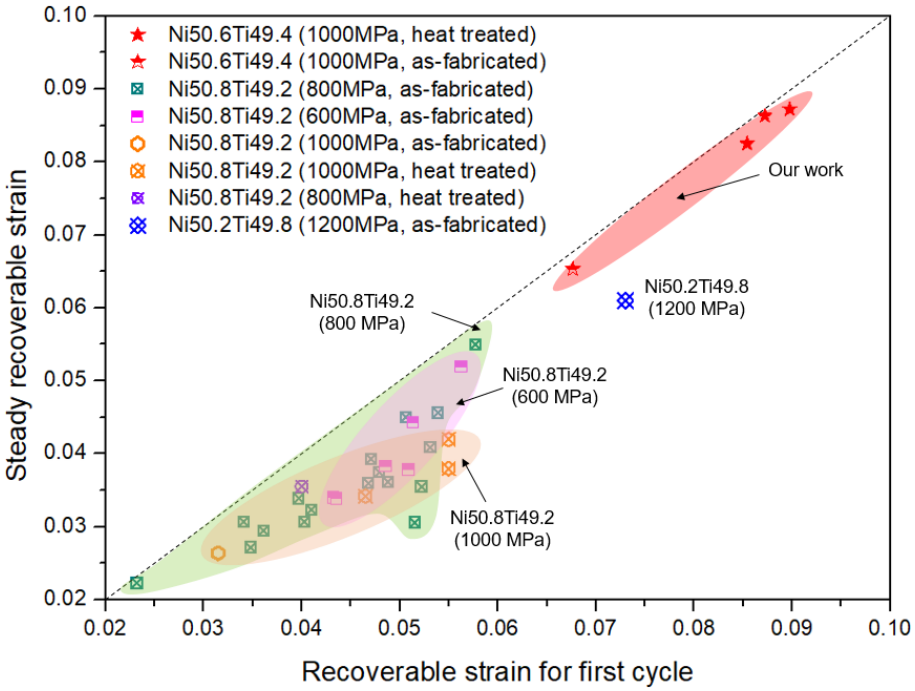

Fig. 13 A summary of steady recoverable strain (obtained under 10 cycles) versus initial recoverable strain (obtained under the first cycle) of LPBF-fabricated Ni-rich NiTi alloys in the compressive loading condition [17, 21, 48-51], including our work (red region).

5. Conclusion

In this work, the effects of aging time on microstructure, phase transformation behavior, superelasticity of LPBF-fabricated Ni-rich NiTi samples were studied systematacially. The following conclusions could be drawn:

(1) For the LPBF-fabricated sample, the microstructure was characterized as B2 phase decorated by semi-coherent $Ti_4Ni_2O_x$ particles and the inhomogeneous Ni concentration. With the aging time, the Ni-rich intermetallic compounds including Ni_3Ti and Ni_4Ti_3 unevenly precipitated from the matrix, simultaneously accompanying with a loss of the semi-coherent relationship between $Ti_4Ni_2O_x$ particle and the matrix. After an overaging treatment, a transformation from $Ti_4Ni_2O_x$ phase to TiO_x phase occurred, with a decrease of the precipitate density due to the growth of precipitates.

(2) With the progress of the precipitation, the Ni concentration and the elastic strain field within the matrix varied, thus resulting in different aged martensitic microstructures. At 20 min, 1 h and 10 h of aging, lath-like martensite, (001) compound twins and <011> type II twins dominated, respectively. Besides, due to the precipitation of coherent Ni_4Ti_3 and the formation of a high density of dislocations, considerable R phase was also observed in the aged microstructure.

(3) Owing to different sensitivities of B19' and R transformations to the variation in Ni concentration and the elastic strain field, temperature-induced phase transformation behavior of the sample mainly experienced a rapid evolution from a single-phase transformation to a multi-stage phase transformation, with the aging time increasing, which could be well explained by the variation in the Landau free energy.

(4) As for deformation-induced transformation behavior, the residual strain experienced a "the roller coaster" change as the aging time increased and the critical stress showed the opposite case. At an optimized aging time, a large compressive recoverable strain of 0.089 and excellent cyclic stability were achieved, which could be attributed to strong orientation texture, $Ti_4Ni_2O_x$ nanoparticle and nanoscale coherent Ni_4Ti_3 precipitate.

Acknowledgement

This work was supported by the financial support from the National Natural Science Foundation of China (No. 52105345, U1930207), and the Fundamental Research Funds for the Central Universities (No. JUSRP122028). Besides, the authors wish to thank the ASTUTE team in Cardiff University for valuable discussions on this work.

Reference

[1] K. Otsuka, X. Ren. Physical metallurgy of Ti–Ni-based shape memory alloys. Prog. Mater Sci. 50 (2005) 511–678.

[2] S. Parvizi, S.M. Hashemi, F. Asgarinia, M. Nematollahi, M. Elahinia, Effective Parameters on the Final Properties of NiTi-based Alloys Manufactured by Powder Metallurgy Methods: A Review. Prog. Mater. Sci. 117 (2020) 100739.

[3] M.H. Elahinia, M. Hashemi, M. Tabesh, S.B. Bhaduri. Manufacturing and processing of NiTi implants: A review. Prog. Mater Sci. 57 (2012) 911–946.

[4] C. Ma, D. Gu, D. Dai, M. Xia, H. Chen, Selective growth of Ni4Ti3 precipitate variants induced by complicated cyclic stress during laser additive manufacturing of NiTi-based composites. Mater. Character. 143 (2018) s191-s196.

[5] W.J. Buehler, J.W. Gilfrich, R.C. Wiley. Effect of low-temperature phase changes on mechanical properties of alloys near composition TiNi. J. Appl. Phys. 34 (1963) 1473-1478.

[6] N. Sharma, K.K. Jangra, T. Raj. Fabrication of NiTi alloy: A review. J. Mater.: Des. Appl. 232 (2018) 250-269.

[7] M. Nishida, C.M. Wayman, T. Honma. Precipitation processes in near-equiatomic TiNi shape memory alloys. Metall. Trans. A 17A (1986) 1505-1515.

[8] J.K. Allafi, X. Ren, G. Eggeler. The mechanism of multistage martensitic transformations in aged Ni-rich NiTi shape memory alloys. Acta Mater. 50 (2002) 793-803.

[9] Y. Zheng, F. Jiang, L. Li, H. Yang, Y. Liu. Effect of aging treatment on the transformation behavior of Ti-50.9 at.% Ni alloy. Acta Mater. 56 (2008) 736-745.

[10] F. Jiang, Y. Liu, H. Yang, L. Li, Y. Zheng. Effect of aging treatment on the deformation

behavior of Ti-50.9 at.% Ni alloy. Acta Mater. 57 (2009) 4773-4781.

[11] D.D. Gu, X. Shi, R. Poprawe, D.L. Bourell, R. Setchi, J. Zhu. Material-structure-performance integrated laser-metal additive manufacturing. Science 372 (2021) 1487.

[12] C. Ma, D. Gu, K. Lin, D. Dai, M. Xia, J. Yang, H. Wang. Selective laser melting additive manufacturing of cancer pagurus's claw inspired bionic structures with high strength and toughness. Appl. Surf. Sci. 469 (2019) 647–656.

[13] S. Li, H. Hassanin, M.M. Attallah, N.J.E. Adkins, K. Essa. The development of TiNi-based negative Poisson's ratio structure using selective laser melting. Acta Mater. 105 (2016) 75-83.

[14] C.L. Tan, J. Zou, S. Li, P. Jamshidi, A. Abena, A. Forsey, R.J. Moat, K. Essa, M.S. Wang, K.S. Zhou, M.M. Attallah. Additive manufacturing of bio-inspired multi-scale hierarchically strengthened lattice structures. Int. J. Mach. Tools Manuf 167 (2021) 103764.

[15] T. DebRoy, H.L. Wei, J.S. Zuback, T. Mukherjee, J.W. Elmer, J.O. Milewski, A.M. Beese, A. Wilson-Heid, A. De, W. Zhang. Additive manufacturing of metallic components – Process, structure and properties. Prog. Mater Sci. 92 (2018) 112–224.

[16] Q. Zhang, S. Hao, Y. Liu, Z. Xiong, W. Guo, Y. Yang, Y. Ren, L. Cui, L. Ren, Z. Zhang. The microstructure of a selective laser melting (SLM)-fabricated NiTi shape memory alloy with superior tensile property and shape memory recoverability. Appl. Mater. Today 19 (2020) 100547.

[17] N.S. Moghaddam, S. Saedi, A. Amerinatanzi, A. Hinojos, A. Ramazani, J. Kundin, M.J. Mills, H. Karaca, M. Elahinia. Achieving superelasticity in additively manufactured NiTi in compression without post-process heat treatment. Sci. Rep. 9 (2019) 41

[18] R.F. Hamilton, T.A. Palmerb, B.A. Bimber. Spatial characterization of the thermal-induced phase transformation throughout as-deposited additive manufactured NiTi bulk builds. Scripta

Mater. 101 (2015) 56–59.

[19] S. Dadbakhsh, B. Vrancken, J.-P. Kruth, J. Luyten, J.V. Humbeeck. Texture and anisotropy in selective laser melting of NiTi alloy. Mater. Sci. Eng., A 650 (2016) 225–232.

[20] S. Saedi, A.S. Turabi, M.T. Andani, N.S. Moghaddam, M. Elahinia, H.E. Karaca. Texture, aging, and superelasticity of selective laser melting fabricated Ni-rich NiTi alloys. Mater. Sci. Eng., A 686 (2017) 1–10.

[21] S. Saedi, A.S. Turabi, M.T. Andani, C. Haberland, H. Karaca, M. Elahinia. The influence of heat treatment on the thermomechanical response of Ni-rich NiTi alloys manufactured by selective laser melting. J. Alloys Compd. 677 (2016) 204-210.

[22] Z.X. Khoo, J. An, C.K. Chua, Y.F. Shen, C.N. Kuo, Y. Liu. Effect of Heat Treatment on Repetitively Scanned SLM NiTi Shape Memory Alloy. Materials 12 (2019) 77.

[23] H.Z. Lu, H.W. Ma, W.S. Cai, X. Luo, Z. Wang, C.H. Song, S. Yin, C. Yang. Stable tensile recovery strain induced by a Ni_4Ti_3 nanoprecipitate in a $Ni_{50.4}Ti_{49.6}$ shape memory alloy fabricated via selective laser melting. Acta Materialia 219 (2021) 117261.

[24] A.H. Ammar, M. Al-Buhairi, A.A.M. Farag, N.M.M. Al-Wajeeh. Influence of heat treatment on the mechanical and electrical characteristics of $Ni_{0.5}Ti_{0.5}$ alloy prepared by electron-beam melting. Physica B 419 (2013) 90–94.

[25] A. Sinha, B. Mondal, P.P. Chattopadhyay. Mechanical properties of Ti–(∼49 at%) Ni shape memory alloy, part II: Effect of aging treatment. Mater. Sci. Eng., A 561 (2013) 344-351.

[26] L.J. Chiang, C.H. Li, Y.F. Hsu, W.H. Wang. Age-induced four-stage transformation in Ni-rich NiTi shape memory alloys. J. Alloys Compd. 458 (2008) 231-237.

[27] B.C. Hornbuckle, X.X. Yu, R.D. Noebe, R. Martens, M.L. Weaver, G.B. Thompson.

Hardening behavior and phase decomposition in very Ni-rich Nitinol alloys. Mater. Sci. Eng., A 639 (2015) 336–344.

[28] T. Ezaz, H. Sehitoglu, H.J. Maier, Energetics of twinning in martensitic NiTi, Acta Mater. 59 (2011) 5893–5904.

[29] D.C. Ren, H.B. Zhang, Y.J. Liu, S.J. Li, W. Jin, R. Yang, L.C. Zhang. Microstructure and properties of equiatomic Ti-Ni alloy fabricated by selective laser melting. Mater. Sci. Eng., A 771 (2020) 138586

[30] H.Z. Lu, L.H. Liu, C. Yang, X. Luo, C.H. Song, Z. Wang, J. Wang,Y.D. Su, Y.F. Ding, L.C. Zhang, Y.Y. Li, Simultaneous enhancement of mechanical and shape memory properties by heat-treatment homogenization of Ti_2Ni precipitates in TiNi shape memory alloy fabricated by selective laser melting, J. Mater. Sci. Tech. 101 (2022) 205-216.

[31] A. Klassen, V.E. Forster, V. Juechter, C. Körner. Numerical simulation of multi-component evaporation during selective electron beam melting of TiAl. J. Mater. Process. Tech. 247 (2017) 280–288.

[32] R. Nagarajan, K Chattopadhyay. Intermetallic Ti_2Ni/TiNi nanocomposite by rapid solidification. Acta Metall. Mater. 42 (1994) 947-958.

[33] V. G. Chuprina, I. M. Shalya. Reactions of TiNi with oxygen. Powder Metall. Met. Ceram. 41 (2002) 85-89.

[34] H. Hou, E. Simsek, T. Ma, N.S. Johnson, S. Qian, C. Cissé, D. Stasak, N.A. Hasan, L. Zhou, Y. Hwang, R. Radermacher, V.I. Levitas, M.J. Kramer, M.A. Zaeem, A.P. Stebner, R.T. Ott, J. Cui, I. Takeuchi. Fatigue-resistant high-performance elastocaloric materials via additive manufacturing. Science 366 (2019) 1116-1121.

[35] G. Fan, W. Chen, S. Yang, J. Zhu, X. Ren, K. Otsuka. Origin of abnormal multi-stage martensitic transformation behavior in aged Ni-rich Ti–Ni shape memory alloys. Acta Mater. 52 (2004) 4351-4362.

[36] R. Nakamura, K. Yoshimi, S. Tsurekawa, Supersaturated vacancies andvacancy complexes in rapidly solidified B2 aluminide ribbons, Mater. Sci. Eng.A 448-451 (2007) 1036-1040.

[37] G. Schoeck, W.A. Tiller, On dislocation formation by vacancy condensation, Philos. Mag. 5 (1960) 43-63.

[38] E. Nes, The mechanism of repeated precipitated on dislocations, Acta Metall.22 (1974) 81-87.

[39] T. Simon, A. Kroger, C. Somsen, A. Dlouhy, G. Eggeler. On the multiplication of dislocations during martensitic transformations in NiTi shape memory alloys. Acta Mater. 58 (2010) 1850-1860.

[40] T. Ezaz, J. Wang, H. Sehitoglu, H. Maier. Plastic deformation of NiTi shape memory alloys. Acta Mater. 61 (2013) 67-78.

[41] D. Stroz, D. Chrobak. Effect of Internal Strain on Martensitic Transformations in NiTi Shape Memory Alloys. Mater. Trans. JIM 52 (2011) 358-363.

[42] N. Zhou, C. Shen, M.F.-X. Wagner, G. Eggeler, M.J. Mills, Y. Wang. Effect of Ni4Ti3 precipitation on martensitic transformation in Ti-Ni. Acta Mater. 58 (2010) 6685–6694.

[43] D. Gu, C.L. Ma, D.H. Dai, J.K. Yang, H.M. Zhang, H. Zhang. Additively Manufacturing Enabled Hierarchical NiTi-based Shape Memory Alloys with High Strength and Toughness. Virtual Phys. Prototyp. 16 (2021) s19-s38.

[44] T. Waitz, V. Kazykhanov, H.P. Karnthaler. Martensitic phase transformations in

nanocrystalline NiTi studied by TEM. Acta Mater. 52 (2004) 137–147.

[45] M. Nishida, C.M. Wayman, A. Chiba. Electron microscopy studies of the martensitic transformation in an aged Ti-51at.%Ni shape memory alloy. Metallography 21 (1988) 275-291.

[46] T. Fukuda, T. Saburi, K. Doi, S. Nenno. Nucleation and self-accommodation of the R-phase in Ti-Ni alloys. Mater. Trans., JIM 33 (1992) 271-277

[47] E.K.H. Salje. Phase transformations in ferroelastic and co-elastic crystals. Cambridge University Press; 1993.

[48] S. Saedi, N.S. Moghaddam, A. Amerinatanzi, M. Elahinia, H.E. Karaca. On the effects of selective laser melting process parameters on microstructure and thermomechanical response of Ni-rich NiTi. Acta Mater. 144 (2018) 552-560.

[49] S. Saedi, S.E. Saghaian, A. Jahadakbar, N.S. Moghaddam, M.T. Andani, S.M. Saghaian, Y.C. Lu, M. Elahinia, H.E. Karaca. Shape memory response of porous NiTi shape memory alloys fabricated by selective laser melting. J. Mater. Sci. Mater. Medic. 29 (2018) 40.

[50] S.E. Saghaian, M. Nematollahi, G. Toker, A. Hinojos, N.S. Moghaddam, S. Saedi, C.Y. Lu, M.J. Mahtabi, M.J. Mills, M. Elahinia, H.E. Karaca. Effect of hatch spacing and laser power on microstructure, texture, and thermomechanical properties of laser powder bed fusion (L-PBF) additively manufactured NiTi. Opt. Laser Tech. 149 (2022) 107680.

[51] H. Meier, C. Haberland, J. Frenzel. Structural and functional properties of NiTi shape memory alloys produced by Selective Laser Melting. Innovative Developments in Virtual and Physical Prototyping, London, 2012, 291-296.

[52] C.L. Ma, M.P. Wu, D.H. Dai, M.J. Xia. Stress-induced heterogeneous transformation and recoverable behavior of laser powder bed fused Ni-rich Ni50.6Ti49.4 alloys without post

treatment. J. Alloys Compd. 905 (2022) 164212.

[53] P. Chowdhury, H. Sehitoglu. A revisit to atomistic rationale for slip in shape memory alloys. Prog. Mater Sci. 85 (2017) 1-42.

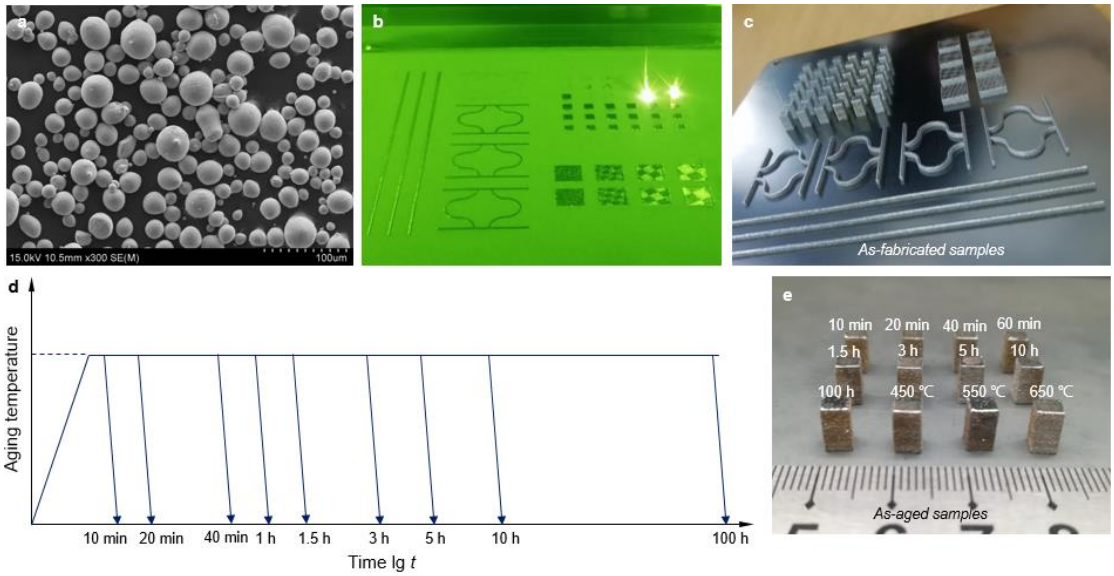

Fig.1 a The raw powder material showing a high degree of sphericity; **b** The LPBF process showing the interaction between laser beam and powder bed; **c** The as-fabricated samples; **d** The aging treatment regime; **e** The as-aged samples.

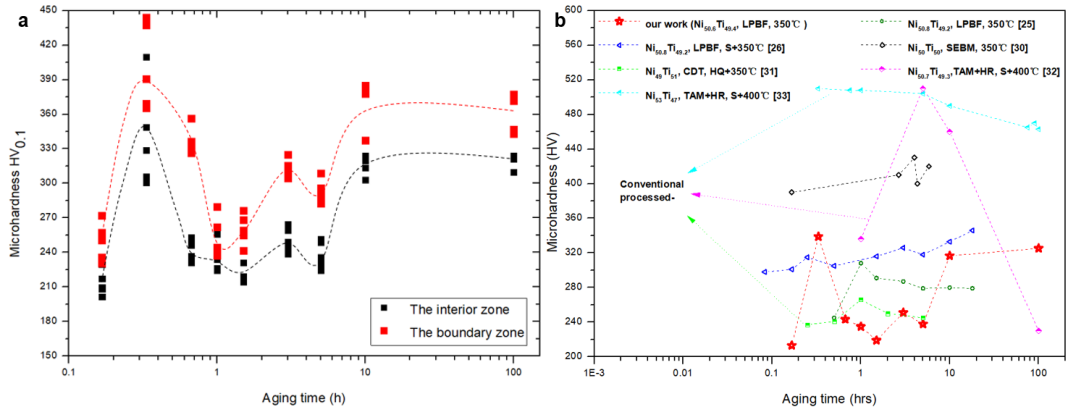

Fig. 2 Microhardness evolution with the aging time. **a** The measured microhardness values in the interior zone and boundary zone of the molten pool at different aging time; **b** Comparisons with other investigations [20, 21, 24-27]. Here, SEBM is selective electron-beam melting, CDT means cold-drawn and tempered, TAM denotes tungsten arc melting; HQ is the homogenized and quenched state, S means solution.

Table 1 A summary about characteristic temperature data (M_s, M_f, A_s *and* A_f) and heat of transformation (Q) from all peaks (peak 1-6 marked in Fig. 3) in the DSC curves of as-fabricated sample and as-aged samples.

Aging time t (h)	Forward martensitic transformation							Reverse martensitic transformation						
	Temperature (°C)				Heat (J/g)			Temperature (°C)				Heat (J/g)		
	M_s^1	M_f^2	M_s^3	M_f^3	Q^1	Q^2	Q^3	A_s^4	A_f^5	A_s^6	A_f^6	Q^4	Q^5	Q^6
0	21.41	-41.6	-	-	18.68	-	-	-	-	-13.2	51.94	-	-	17.30
0.333	67.85	11.70	-	-	20.17	-	-	-	-	64.79	112.22	-	-	16.38
1	47.62	31.89	-	-	8.28		0	36.51	47.91	73.03	95.24	9.49		1.85
3	51.23	36.47	-	-	11.02		0	39.96	51.07	73.91	99.17	9.35		3.66
5	52.78	38.58	-	-	9.12		0	42.26	52.18	82.95	95.52	9.12		0.87
10	54.99	41.13	8.50	-7.2	9.35		0.31	45.38	53.92	85.83	96.79	5.30		0.65

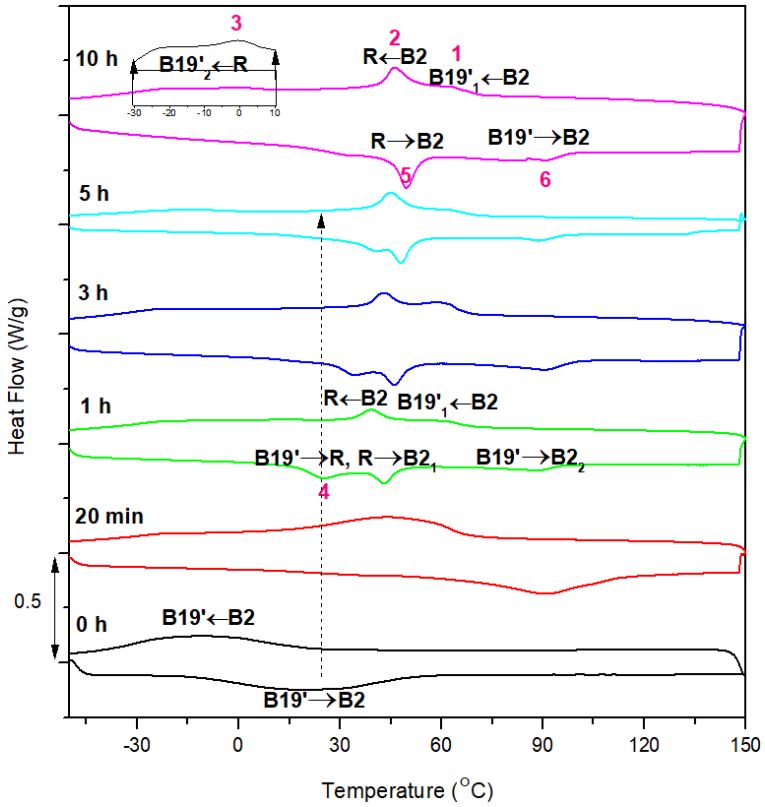

Fig. 3 DSC curves of the Ni-rich NiTi samples obtained at different aging times. 1, 2 and 3 denote the transformation peaks emerging in the forward transformation process; 4, 5 and 6 denote the transformation peaks emerging in the reverse transformation process.

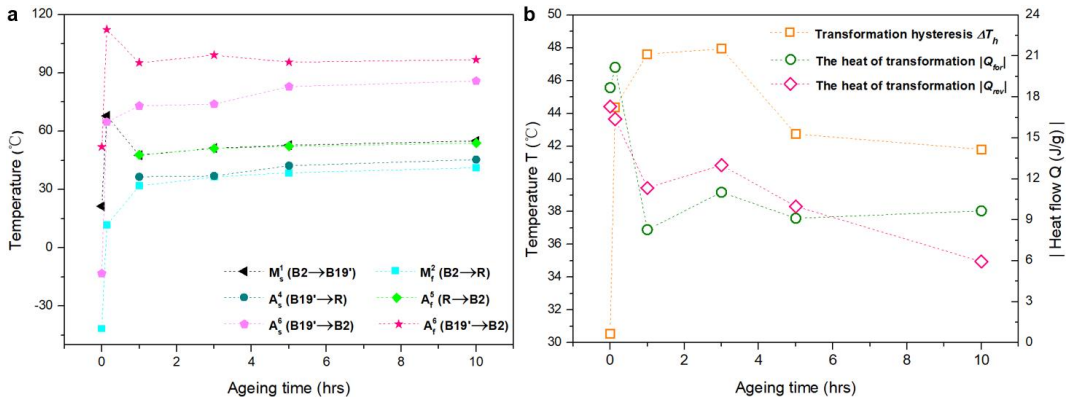

Fig. 4 Effect of aging time on (**a**) the characteristic temperatures, (**b**) transformation hysteresis and the heat of the forward and reverse transformation.

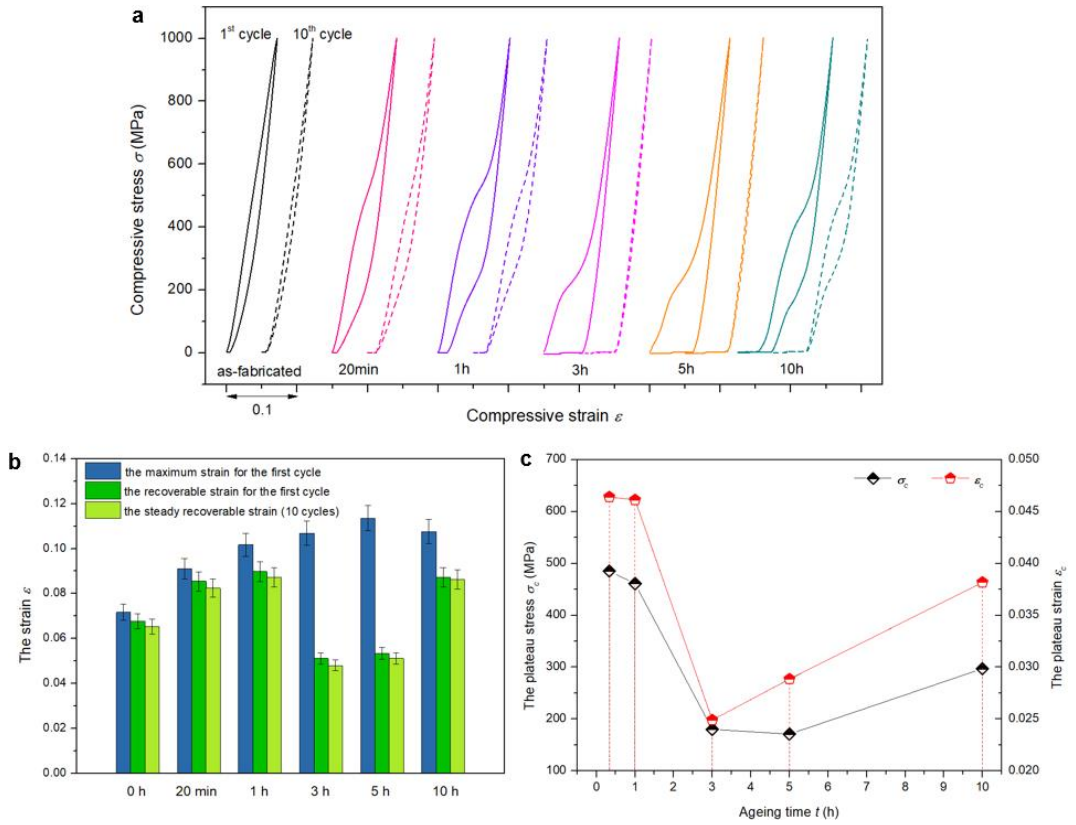

Fig. 5 The superelastic behavior of as-fabricated sample and as-aged samples. **a** The cyclic compressive loading-unloading curves; **b** The variations in the maximum strain and the recoverable strain at different aging time; **c** The evolutions of the plateau stress σ_c and the plateau strain ε_c.

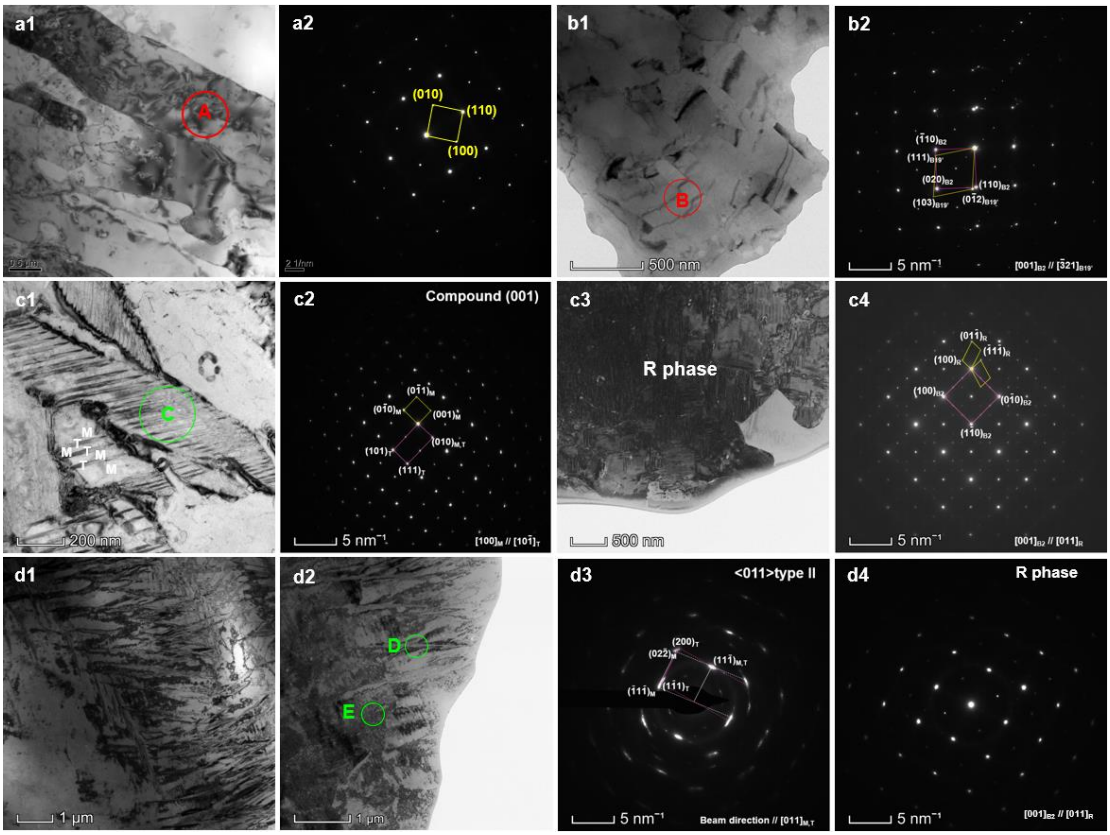

Fig. 6 TEM images and the corresponding SADPs of the microstructure in the as-fabricated and as-aged samples. **a1**-**a2** as-fabricated sample, **a1** the TEM image and **a2** the SADP of region A; **b1**-**b2** 20 min aged sample, **b1** the TEM image and **b2** the SADP of region B; **c1**-**c4** 1 h aged sample, **c1** the TEM image showing the fine acicular martensitic twin lamellas, **c2** the SADP of region C, **c3** the TEM image showing the R phase and **c4** the corresponding SADP; **d1**-**d4** 10 h aged sample, **d1** and **d2** the TEM images captured in two different zones, **d3** and **d4** the SADPs of region D and region E, respectively.

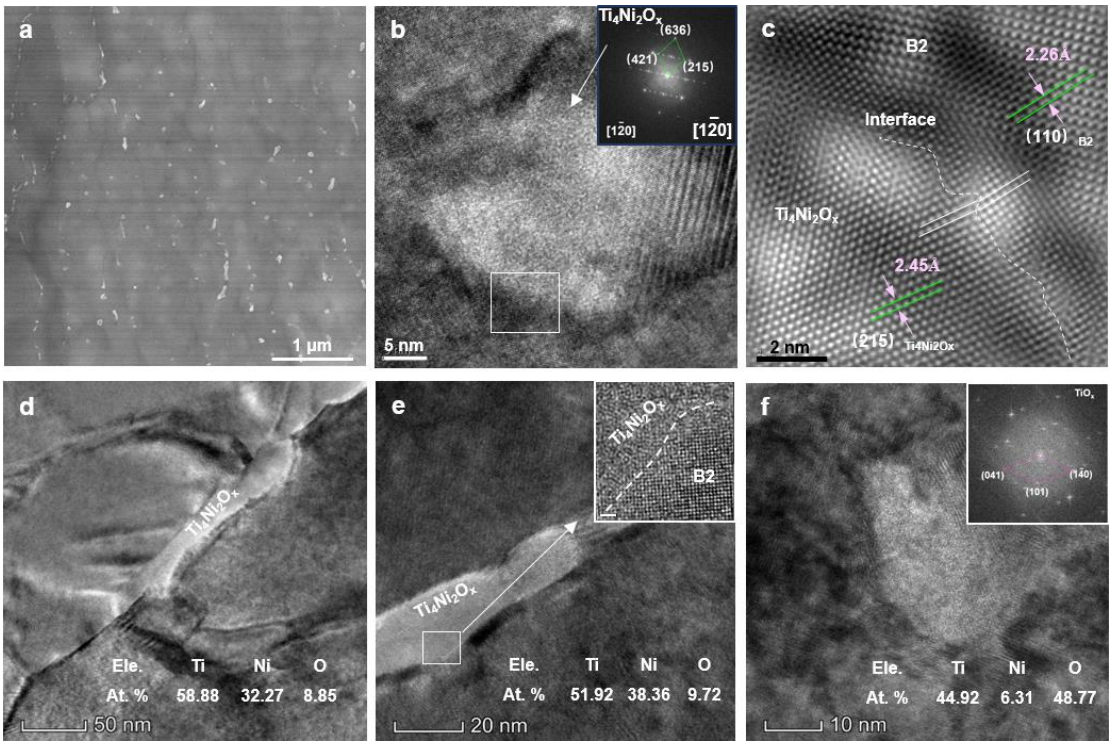

Fig. 7 Morphology and chemical content of the $Ti_4Ni_2O_x$ nanoparticle in different conditions. **a-c** the $Ti_4Ni_2O_x$ nanoparticle existing in the as-fabricated sample and **a** the SEM image showing the distribution feature of $Ti_4Ni_2O_x$ nanoparticles along the grain boundaries, **b** the HR-TEM image showing a single $Ti_4Ni_2O_x$ nanoparticle, **c** the inverse FFT images showing the interface structure. **d-f** corresponding to the $Ti_4Ni_2O_x$ nanoparticle observed in the 20-min, 1-h and 10-h aged samples, respectively.

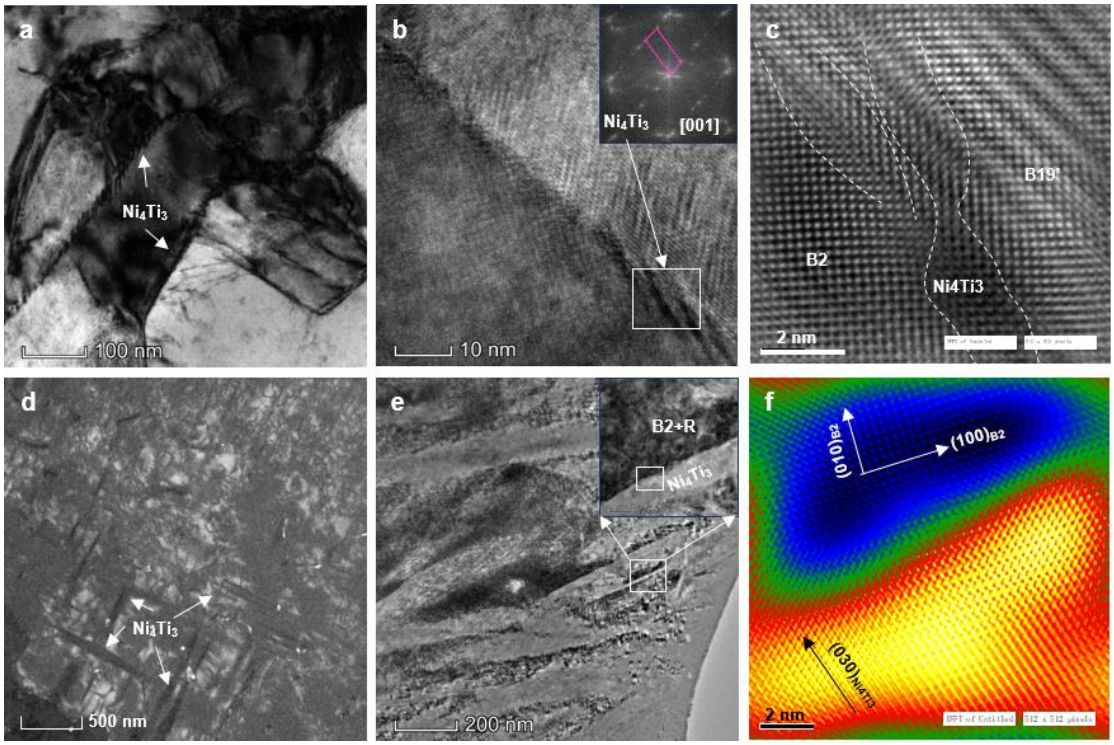

Fig. 8 TEM characterization of the Ni_4Ti_3 precipitate at different aging time. **a-c** the HR-TEM, FFT and inverse FFT images of Ni_4Ti_3 precipitates at the B2 grain boundaries in the 20 min aged sample; **d** the dark-field TEM image of Ni_4Ti_3 precipitates in the 1 h aged sample; **e** and **f** the HR-TEM and inverse FFT images of Ni_4Ti_3 precipitates in the 10 h aged sample.

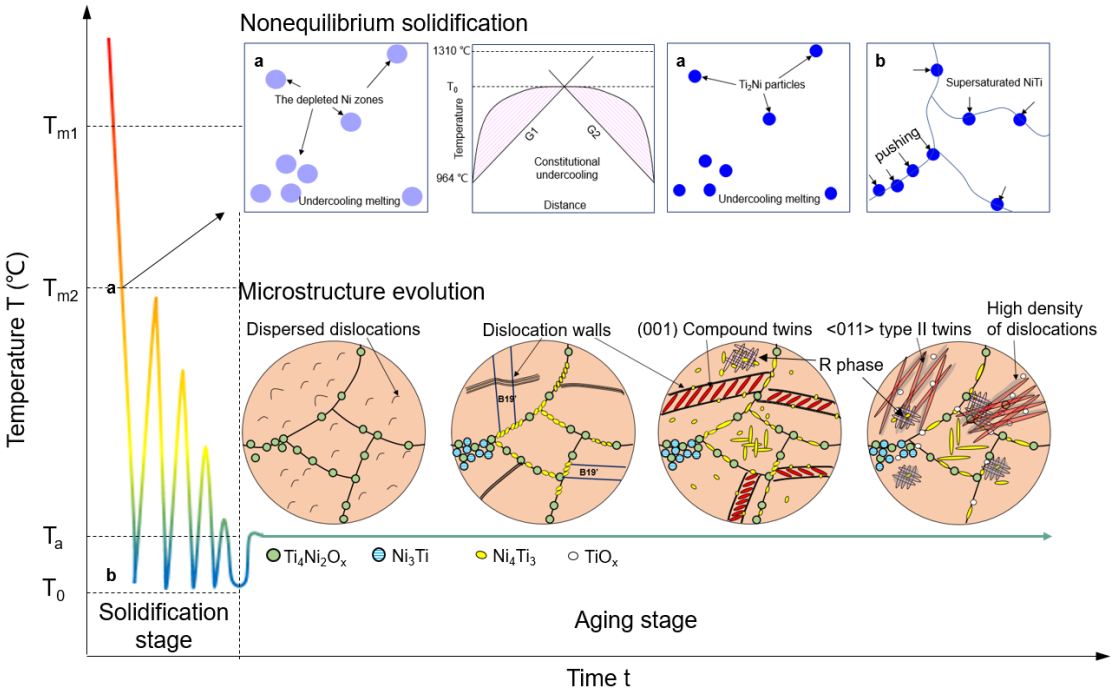

Fig. 9 The thermal history and evolution process of microstructures during the LPBF and subsequent aging treatment. Tm_1, melting temperature of NiTi phase, Tm_2, melting temperature of Ti_2Ni phase, T_a, aging temperature and T_0, ambient temperature.

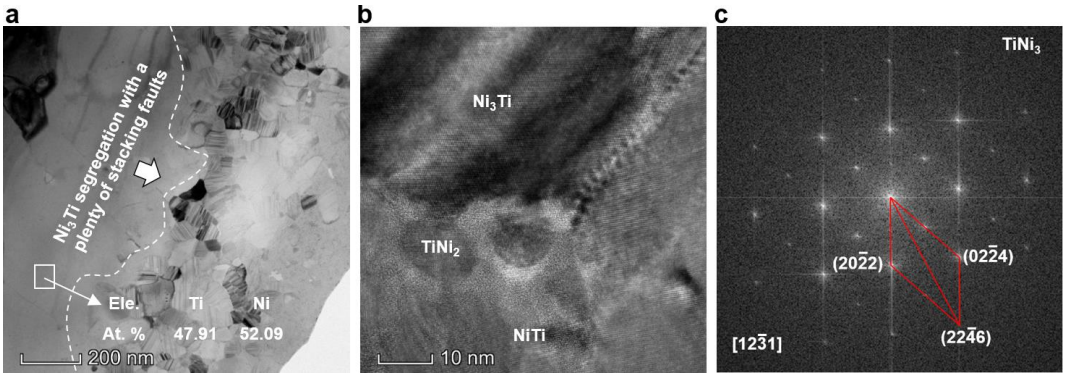

Fig. 10 TEM characterization of Ni_3Ti particles. **a** TEM images, **b** the local high-resolution TEM image and **c** the corresponding FFT image of the Ni_3Ti precipitate in the 20 min aged sample.

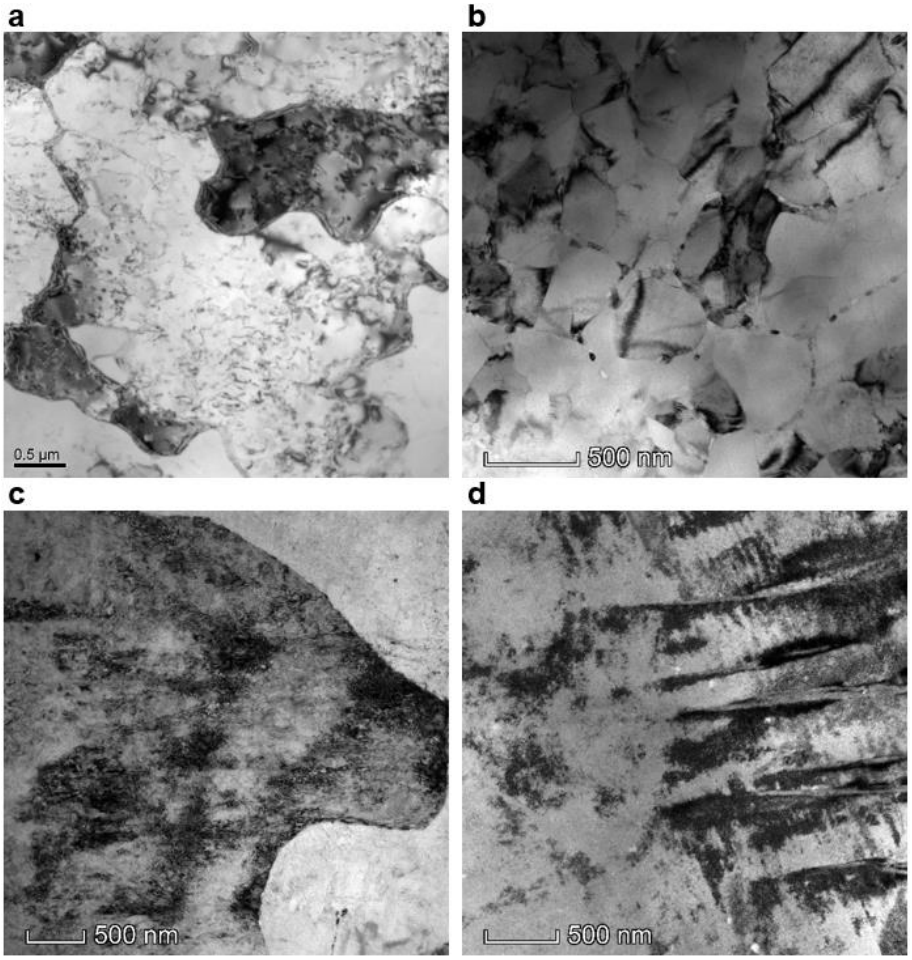

Fig. 11 TEM images of dislocations observed in the LPBF-fabricated and aged NiTi samples. **a** as-fabricated sample, **b** 20 min aged sample, **c** 1 h aged sample, and **d** 10 h aged sample.

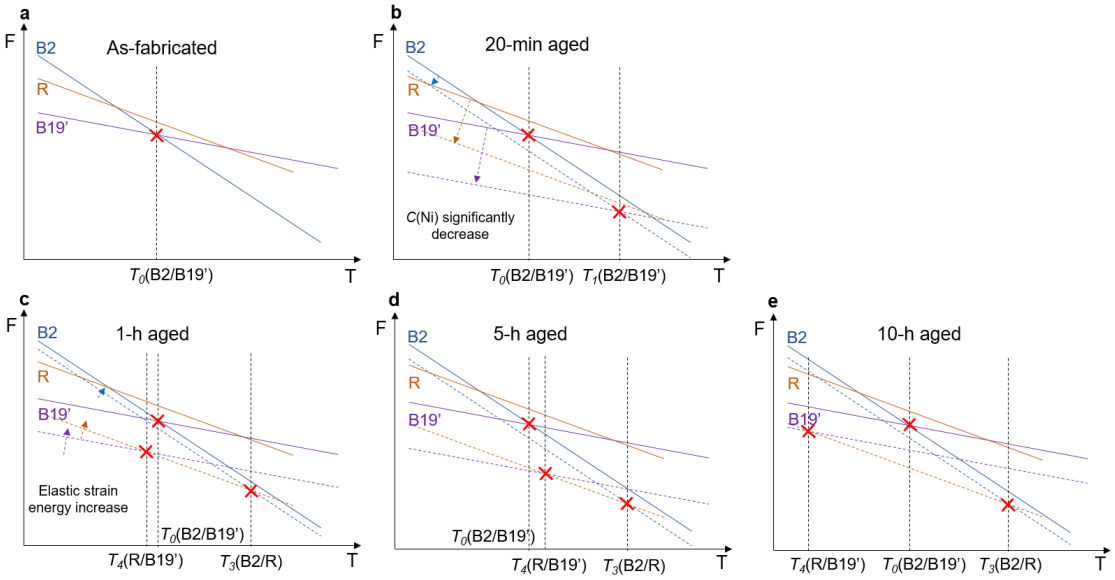

Fig. 12 The Landau free energy of B2, B19' and R phases at different aging conditions, disclosing the change in the reasonable transformation path and temperature.

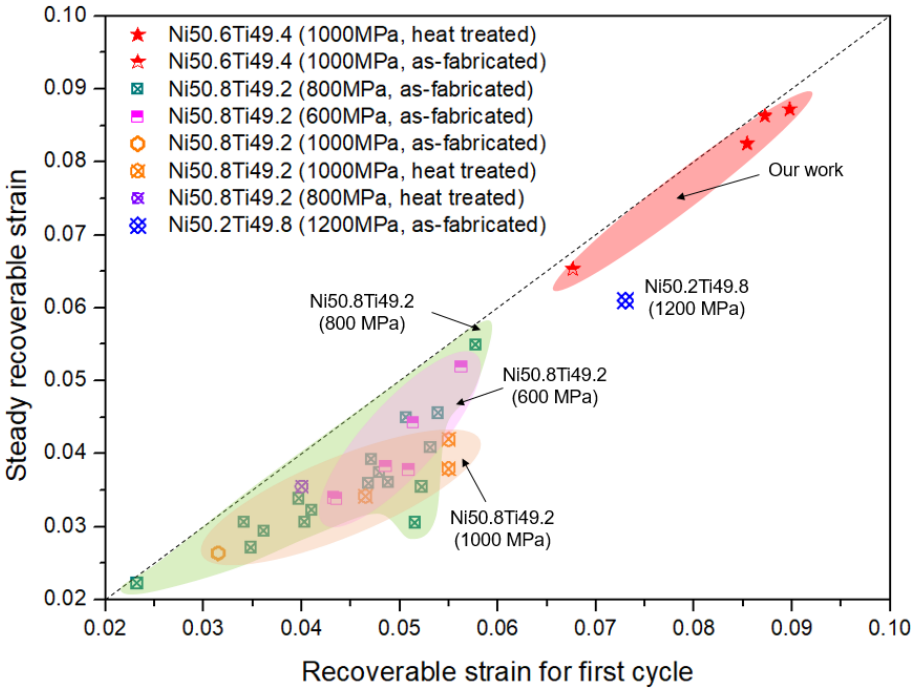

Fig. 13 A summary of steady recoverable strain (obtained under 10 cycles) versus initial recoverable strain (obtained under the first cycle) of LPBF-fabricated Ni-rich NiTi alloys in the compressive loading condition [17, 21, 48-51], including our work (red region).